Geophysical Journal International

Geophys. J. Int. (2023) **232,** 705–724
Advance Access publication 2022 September 12
GJI Seismology
https://doi.org/10.1093/gji/ggac359

Mineralogy, fabric and deformation domains in D″ across the southwestern border of the African LLSVP

Angelo Pisconti [1], Neala Creasy [2], James Wookey,[3] Maureen D. Long[4] and Christine Thomas[1]

[1] *Institut für Geophysik, Westfälische Wilhelms Universität Münster, Corrensstraße* 24, 48149 *Münster, Germany. E-mail:* pisconti@uni-muenster.de
[2] *Los Alamos National Laboratory, Los Alamos, NM 87545, USA*
[3] *School of Earth Sciences, University of Bristol, Bristol BS8 1RL, UK*
[4] *Department of Earth and Planetary Sciences, Yale University, New Haven, CT* 06520, *USA*

Accepted 2022 September 3. Received 2022 September 1; in original form 2021 December 21

SUMMARY

Recent advances in seismic anisotropy studies that jointly use reflections and shear wave splitting have proven to place tight constraints on the plausible anisotropic and deformation scenarios in the D″ region. We apply this novel methodology to a large area of the D″ region beneath the South Atlantic, in proximity to and within the African large low seismic velocity province (LLSVP). This area of the mantle is characterized by a transition from fast to slow seismic velocity anomalies and it is thought to be the location of deep-seated plumes responsible for hotspot volcanism. Attempting to probe mantle composition and deformation along the LLSVP borders may provide key information on mantle dynamics. By analysing seismic phases sampling this region, we detect a D″ discontinuity over a large area beneath the South Atlantic, with inferred depth ranges ∼170 to ∼240 km above the core–mantle boundary. We find evidence for a D″ reflector within the area of the LLSVP. Shear wave splitting observations suggest that anisotropy is present in this region of the mantle, in agreement with previous studies that partially sampled this region. We model the observations considering lattice- and shape-preferred orientation of materials expected in the D″ region. A regional variation of mineralogy, phase transition boundaries, and deformation direction is required to explain the data. We infer two distinct domains of mineralogy and deformation: aligned post-perovskite outside the LLSVP and aligned bridgmanite within the LLSVP. The scenario depicted by this study agrees well with the current hypotheses for the composition of the LLSVP and with the prevalence of vertical deformation directions expected to occur along the LLSVPs borders.

Key words: Composition and structure of the mantle; Phase transitions; Atlantic Ocean; Seismic anisotropy.

1 INTRODUCTION

The lowermost mantle beneath the South Atlantic Ocean is seismically imaged as a transition from fast to slow velocity regions going from west to east (e.g. Ni & Helmberger 2001; Amaru 2007; Ritsema *et al.* 2011; Hosseini *et al.* 2018). The fast region is usually associated with subducted oceanic lithosphere now residing at the core–mantle boundary (CMB), as proposed by several studies (Richards & Engebretson 1992; Grand 1994; Ni & Helmberger 2001; van der Meer *et al.* 2018) while the low velocity region, appearing in all global tomographic models (e.g. Fig. 1), is related to the African Large Low Seismic Velocity Province (LLSVP; e.g. Ritsema *et al.* 1999; Ni & Helmberger 2001, 2003a, b; Wang & Wen 2004, 2007a; Garnero *et al.* 2016). The African LLSVP seems to extend upwards from the base of the mantle to the mid-mantle, perhaps reaching the upper mantle beneath eastern Africa, and thought to be the cause for flood basalts and rifting along the East African Rift system (e.g. Ritsema *et al.* 1999; Hansen *et al.* 2012; Civiero *et al.* 2015; Garnero *et al.* 2016; Chang *et al.* 2020).

In general, the LLSVPs beneath Africa and the Pacific Ocean cover about 20 per cent of the CMB area (Burke *et al.* 2008) and are closely linked to the dynamics of the Earth's deep mantle. The African LLSVP has been related to deep mantle plumes feeding Large Igneous Provinces (LIPs) through geological time (Burke & Torsvik 2004; Burke *et al.* 2008; Torsvik *et al.* 2008; Dziewonski *et al.* 2010), but the South Atlantic also hosts present-day hotspots and volcanic islands, such as Ascension and Tristan de Cunha (Courtillot *et al.* 2003; Torsvik *et al.* 2008). Due to its large size, the

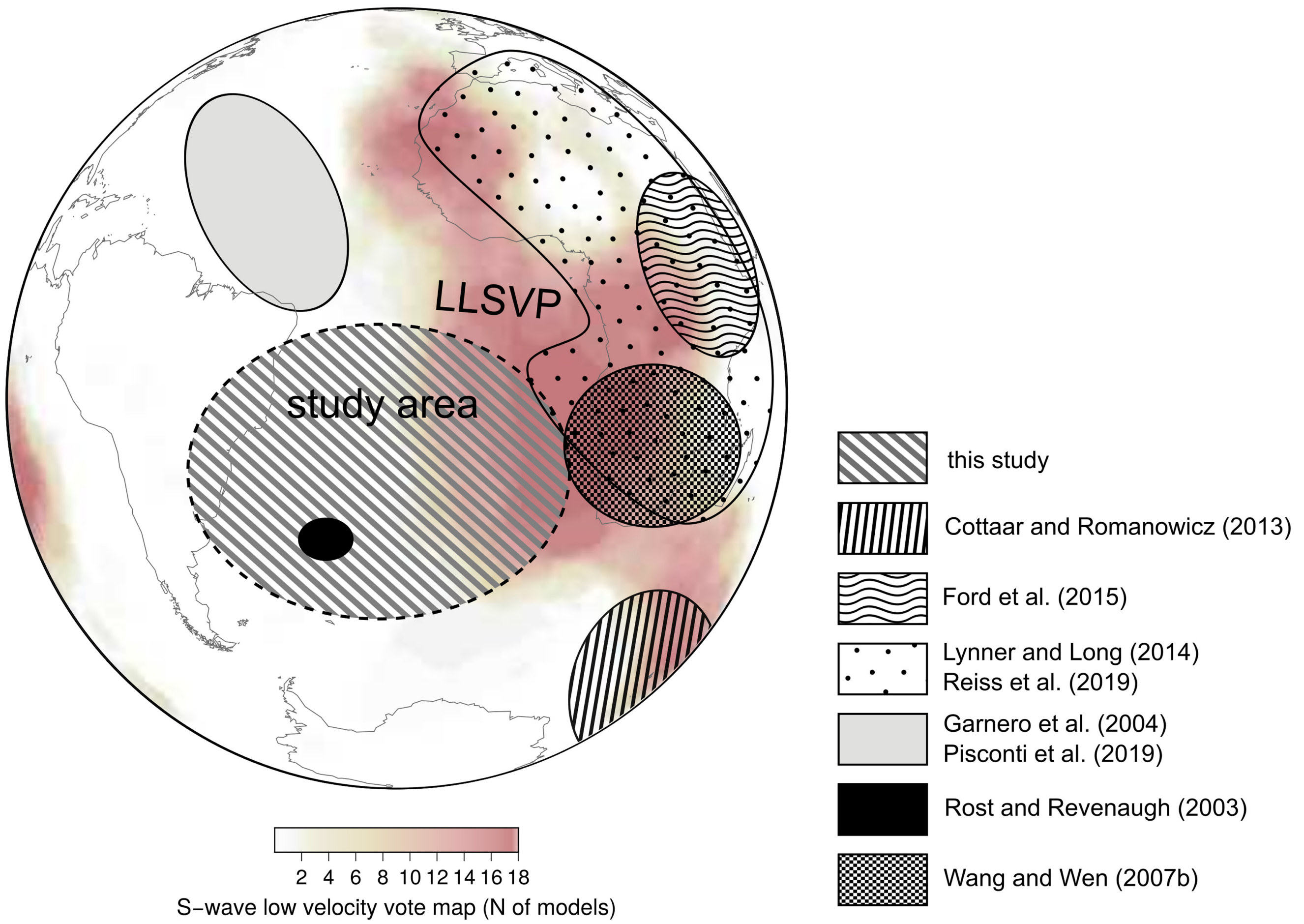

Figure 1. Study area covering the South Atlantic and part of the African LLSVP. The *S*-wave vote map for low velocities (Shephard *et al.* 2017) in the background was computed using tomographic models incorporated in SubMachine (Hosseini *et al.* 2018). The colour bar indicates the number of tomographic models which agree in finding a low velocity for each point of the map. Shaded areas show region of previous studies (see text for more detail).

LLSVP might also influence heat flux across the CMB, thereby affecting the geomagnetic field (Gubbins *et al.* 2008; Mound *et al.* 2019) and possibly causing the South Atlantic Anomaly (e.g. Amit *et al.* 2015; Tarduno *et al.* 2015), a prominent feature in the Earth's magnetic field.

Despite their geodynamic importance, the precise location of the LLSVP borders is not well constrained, with controversial results particularly for the edges of the African LLSVP (see Garnero *et al.* 2016; McNamara 2019). In addition, the density and mineralogy of the LLSVP are not well constrained yet (e.g. Koelemeijer 2021; Vilella *et al.* 2021). It is crucial to infer their geographical location, composition and structure, since they impact whole Earth dynamics and evolution, and are linked to superficial magmatism and plate tectonics (see the recent work by Niu 2018; McNamara 2019; Chang *et al.* 2020; Koelemeijer 2021). Furthermore, LLSVPs may influence flow in the lowermost mantle (e.g. Cottaar & Romanowicz 2013; Ford *et al.* 2015; Tommasi *et al.* 2018; Reiss *et al.* 2019; Li 2020; Chandler *et al.* 2021).

The observation of seismic anisotropy provides a way to infer and locate deformation and flow direction at different depths in the mantle (e.g. Silver & Chan 1991; Savage 1999; Long & Silver 2009; Nowacki *et al.* 2011; Mainprice 2015; Maupin & Park 2015; Romanowicz & Wenk 2017). Observations of shear wave splitting for seismic phases travelling in the lowermost mantle, together with mineral physics constraints, have helped in the estimation of the style and degree of anisotropy at the bottom of the mantle (the D″ region, Bullen 1949) and in retrieving scenarios of deformation around the CMB (e.g. Kendall & Silver 1996, 1998; Wookey & Kendall 2007; Long & Silver 2009; Nowacki *et al.* 2010, 2011; Mainprice 2015; Romanowicz & Wenk 2017).

Several studies have targeted anisotropy within and around the African LLSVP (see Fig. 1). In a recent collection of worldwide shear wave splitting measurements for lowermost mantle anisotropy, Creasy *et al.* (2019) showed that the South Atlantic region is poorly covered, with only one study of Wang & Wen (2007b). Using SK(K)S splitting, Wang & Wen (2007b) found complex anisotropy within the African LLSVP and its border, with splitting delay times of ∼1 s and fast polarization directions changing over small distances. They concluded that alignment of lowermost mantle minerals, due to varying mantle flow pattern, can explain their results. Moreover, no ScS splitting observations have been published for the South Atlantic. The ScS waves experience splitting when traversing the D″ region and the D″ splitting contribution can be isolated from upper mantle anisotropy with S-ScS differential splitting measurements (e.g. Wookey *et al.* 2005; Wookey & Kendall 2008; Nowacki *et al.* 2010; Pisconti *et al.* 2019).

Across the southern edge of the African LLSVP, off the coast of Antarctica, waveform modelling of diffracted S_{diff} waves indicates a complex pattern of anisotropy due to the presence of the LLSVP border (Cottaar & Romanowicz 2013). Outside the LLSVP, seismic anisotropy is strong and possibly due to alignment of post-perovskite (e.g. Murakami *et al.* 2004), while it rotates at the border of the LLSVP and seems to decrease or be absent within the LLSVP. This behaviour might indicate that the flow in the deep mantle is influenced by the LLSVPs (McNamara & Zhong 2005; Garnero & McNamara 2008; Cottar & Romanowicz 2013). On the opposite side of the African LLSVP, beneath Eastern Africa, Lynner & Long (2014) also found a weakening of SKS-SKKS differential splitting towards the interior of the LLSVP, while Ford *et al.* (2015) used ScS and SKS-SKKS splitting and suggested that the LLSVP edge might deflect the mantle flow upwards. Their observations are consistent with alignment of post-perovskite along the [100] crystallographic axis, but other scenarios might match their findings. Recently, Reiss *et al.* (2019) collected a large data set of SKS-SKKS splitting discrepancies and mapped changes in the flow geometry within and around the African LLSVP, but they find that various scenarios can explain their data.

Overall, studies of splitting-based seismic anisotropy provide observational constraints on the dynamics and mineralogy of the deep mantle. However, discriminating between different causes for anisotropy, mineralogy and mantle flow requires sampling the chosen geographical region with crossing paths. As suggested by Nowacki *et al.* (2011), multiple distinct crossing paths can distinguish azimuthal anisotropy, such as orthorhombic symmetry (e.g. post-perovskite). With present-day distribution of seismic stations, one often deals with large azimuth gaps in the D″ seismic coverage and this limits our ability to investigate low symmetry media. Therefore, constraining azimuthal anisotropy remains challenging.

Besides shear wave splitting, an alternative way to explore mineralogy and flow is the use of seismic reflections from discontinuities in the mantle (Thomas *et al.* 2011; Saki *et al.* 2018; Pisconti *et al.* 2019). Reflections of *P* and *S* waves from D″ discontinuity have been found in many places, revealing physical parameters of the D″ region such as thickness, velocity jumps, topography, and composition (see Cobden *et al.* 2015; Jackson & Thomas 2021, for recent reviews). As shown by Thomas *et al.* (2011), mapping azimuthal variation of reflection coefficients of D″ reflected waves provides a powerful tool to test mineralogy, phase transformation, deformation direction and slip systems.

Pisconti *et al.* (2019) extended this method to use reflection polarity data for *P* and *S* waves combined with shear wave splitting through both modelling and observations. This approach provides tighter constraints on anisotropy beneath the Central Atlantic using a single path direction (Pisconti *et al.* 2019). The best-fitting model of Pisconti *et al.* (2019) consists of a phase transformation from bridgmanite to post-perovskite [100](010) and deformation pointing towards the African LLSVP. This approach of using diverse seismic phases is more efficient than using only one type of measurements (i.e. splitting) but with different azimuths (Creasy *et al.* 2019). Following this, Creasy *et al.* (2021) extended an existing data set of splitting and polarity measurements for seismic waves cross-sampling the lowermost mantle beneath Siberia, by including SK(K)S and PKS splitting measurements for a tight constraint on deformation and mineralogy in this region. Overall, these studies have shown that the combination of seismic phases and methodologies is an efficient way to place constraints on low symmetry anisotropy, even in poorly sampled regions with large azimuthal gaps.

Looking at the geographical distribution of D″ studies (Fig. 1), one finds that the South Atlantic and the region below South Africa have yielded few observations of D″ reflected waves (Wysession *et al.* 1998; Cobden *et al.* 2015; Lay 2015; Jackson & Thomas 2021). To our knowledge, the only published study on a D″ reflector beneath the South Atlantic is by Rost & Revenaugh (2003) (Fig. 1), who used bottom side reflections of PK^dKP (a PKKP wave that is reflected at the mid-point from the underside of D″ discontinuity, see also Fig. 2); their work place the reflector ~300 km above the CMB. Weber & Körnig (1990, 1992) analysed a global data set using the International Seismological Center (ISC) bulletin and found no lowermost mantle reflections in the South Atlantic, indicating that either there was no coverage or that there is possibly no D″ discontinuity present at locations very close to those tested by Rost & Revenaugh (2003). However, Pisconti *et al.* (2019) have shown that a complex behaviour of reflected waves can be generated from an anisotropic D″, leading to observations and non-observations of D″ reflections within a narrow range of azimuth–distance combinations. Therefore, the lack of observed reflections does not necessarily imply the absence of a reflector.

The situation outlined above illustrates the importance and complexity of the D″ region beneath the South Atlantic but also illuminates the current poor data coverage of this area, especially in terms of reflections and splitting observations. Motivated by the recent advances in constraining seismic anisotropy in the D″ region, particularly the insights gained by the combination of methods (reflection and splitting; Pisconti *et al.* 2019; Creasy *et al.* 2019, 2021), we extend the region covered by Pisconti *et al.* (2019) to sample the D″ region outside and inside the African LLSVP. We intend to (i) detect and explore PdP and SdS reflections, (ii) measure ScS splitting parameters and (iii) model these observations jointly in terms of plausible mineralogy and deformation settings. We test whether differences in main mineralogical composition and deformation scenarios occur across the southwestern border of the African LLSVP, since these factors may play a role in the scenarios for the origin and formation of the LLSVPs (e.g. Deschamps *et al.* 2012; Vilella *et al.* 2021).

2 DATA SET

In this study, we collected a large data set from the International Federation of Digital Seismograph Networks (FDSN), aiming to detect reflected waves from the D″ layer, such as PdP and SdS phases (e.g. Weber 1993), and measure splitting parameters of ScS waves (e.g. Wookey *et al.* 2005) sampling the lowermost mantle beneath the South Atlantic. Ray paths in the Earth for these waves in the relevant distance ranges are shown in Fig. 2(a). The arrays used in this study are mainly deployed in Africa and South America (Fig. 2b), while the events are distributed along the subduction zones and mid-ocean ridges around the South Atlantic (Fig. 2b). Event locations were taken from the National Earthquake Information Center (NEIC) catalogue. Lists with networks and events used in this study are provided in the Supporting Information (Tables S1 and S2).

We explore an epicentral distance range from 50° to 80°, extending the search for observations, and the consequent modelling, to shorter distances than Pisconti *et al.* (2019) who explored a distance range from 60° to 80°. In principle, other distances and seismic phases could be investigated when simultaneously looking at both D″ reflections and splitting phenomena, using core phases, that is PK^dKP, SK(K)S, and S_{diff} waves. Indeed, Rost & Revenaugh (2003) observed D″ bottom-side reflections (PK^dKP) in the South Atlantic (see Fig. 1). However, such observations of PK^dKP are difficult to observe due to their very small amplitudes and, furthermore, to sample a common D″ geographical area, the PK^dKP reflection and

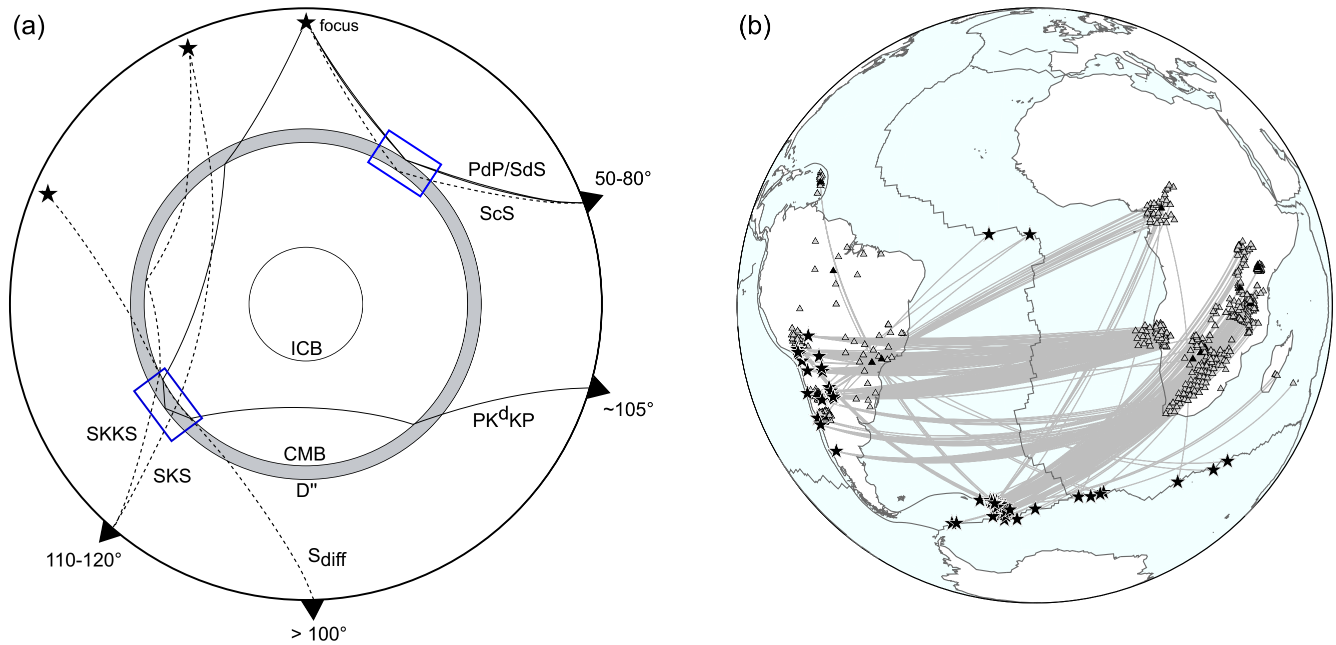

Figure 2. (a) Ray paths of the major seismic phases used to detect the D″ discontinuity with reflected waves (i.e. PdP/SdS and PK^{d}KP, solid lines) and measure splitting parameters (ScS, SKS, SKKS, S$_{diff}$, dashed lines) in the lowermost mantle. Black stars indicate earthquake foci and black triangles indicate seismic stations at the relevant distances. Ray paths are traced using the PWDK model of Weber & Davis (1990) for events at depth of 200 km. The D″ region is represented as a grey-coloured layer with thickness of about 300 km. Note that in the distance range 50–80° both reflections and splitting from a common D″ location (blue box) can be observed using the same source–receiver configuration. (b) Events (black stars), stations (grey triangles) and ray paths (grey lines) used in this study to probe the lowermost mantle beneath the South Atlantic. Only the ray paths to the central station (black triangles) of the arrays are shown in the case of reflection(s), while, for splitting measurements, individual ray paths for each event-station pair are shown.

the splitting of S$_{diff}$ and SK(K)S would have to be observed at different source and receiver locations (see Fig. 2a), posing a technical challenge. Thus, this possibility remains a challenging alternative for applying our strategy of looking at anisotropy; we therefore refrain from using it here. Nevertheless, in some cases, multiple data sets including a wide diversity of seismic phases, such as PdP, SdS, ScS, SK(K)S and PKS, can be used and are very effective, as shown in the recent study of D″ anisotropy beneath Siberia (Creasy *et al.* 2021).

Even though the area investigated in this work offers many potentially usable events, given the presence of subductions beneath South America and South Sandwich Islands, we mainly restricted the analysis to events with depth larger than 50 km. In general, deep events usually have a more impulsive waveform, which allows for a better resolution of the slowness of the PdP and SdS phases by avoiding the interference with depth phases of the direct P/S phases. Therefore, the inspection of waveforms and polarities after the stacking process is facilitated when considering deep events (e.g. Rost & Thomas 2002; Thomas *et al.* 2011; Pisconti *et al.* 2019). In addition, source side shear wave splitting is generally expected to decrease with depth (e.g. Wookey *et al.* 2005; Long & Silver 2009; Nowacki *et al.* 2011), although there are observations of significant seismic anisotropy in the subduction zones even for deep events (e.g. Wookey *et al.* 2005; Rokosky *et al.* 2006; Nowacki *et al.* 2015). In the attempt to search for crossing paths, which would better constrain anisotropy, we also collected a few shallower events that occurred mainly along the mid-Atlantic and Southwest Indian Ocean ridges (Fig. 2b). Events along the mid-ocean ridges have been used previously to constrain D″ anisotropy while correcting for upper mantle contribution using differential S-ScS splitting measurements (e.g. Nowacki *et al.* 2010).

Preliminary processing and a check for good quality signals (clear and impulsive first arrival of *P* and *S* waves) reduced the number of usable earthquakes. This reduction of the size of data sets is common when targeting the deep Earth and, combined with source-to-receiver restrictions (e.g. event distance and depth requirements), consequently reduces availability of crossing paths in the chosen region. However, as found by Pisconti *et al.* (2019), this sparsity of data can be compensated for by the combination of methods (reflection and splitting).

In total, we analysed 79 event-array pairs in search for PdP and SdS reflections and 268 event–station pairs for measuring S-ScS splitting. Like other studies focusing on D″ seismic signals (e.g. Thomas *et al.* 2011; Cobden & Thomas 2013; Pisconti *et al.* 2019; Reiss *et al.* 2019; Wolf *et al.* 2019), we filtered our recordings using a Butterworth bandpass filter with corner periods 1, 3, 10 and 15 s for the *P* waves and 3, 6, 15 and 25 s for the *S* waves.

3 OBSERVATIONS

3.1 Observation of reflection polarity

To search for PdP and SdS reflected waves, we used array seismology techniques as shown in other studies (e.g. Weber & Davis 1990; Weber 1993; Thomas *et al.* 2002, 2004a, b, 2011; Kito *et al.* 2007; Cobden & Thomas 2013; Pisconti *et al.* 2019). In general, waveform stacking across an array allows the detection of signals with low amplitude, as stacking usually decreases incoherent noise and permits a slowness-based seismic phases distinction (Muirhead & Datt 1976; Rost & Thomas 2002, 2009; Schweitzer *et al.* 2012). To reduce the effect of local structures and topography beneath the arrays, prior to stacking, we performed a static correction on the direct P and S reference phases (e.g. Jacobeit *et al.* 2013).

For all available events, we computed and manually inspected the vespagrams for the vertical and transverse component for *P* and SH waves, respectively. In total, we retained 30 good quality vespagrams for the vertical component and 49 for the transverse component. We found 12 PdP observations and 8 SdS observations (Figs 3 and 4 and Tables S3 and S4). These data represent the first-time detection of a D″ discontinuity over a large area beneath the South Atlantic, apart from the localized findings of Rost & Revenaugh (2003). In Figs 3 and 4, we also show some of the vespagrams displaying PdP and SdS reflections, with reflection points located in the lowermost mantle across a large area from South America to South Africa. This configuration has the potential to provide information from outside the LLSVP via the border to within the African LLSVP. Our data do not show any evidence of a second reflector in the D″ region, as reported in previous studies targeting other areas (e.g. Thomas *et al.* 2004a, b, 2011; Hutko *et al.* 2006; Lay *et al.* 2006; van der Hilst *et al.* 2007).

Several vespagrams with a good quality of the stacked signal (clearly visible P, PcP and S, ScS phases) did not show PdP or SdS phases (Figs 3 and 4). We labelled those samples as non-observations (white circles in maps of Figs 3 and 4). Weber & Körnig (1990, 1992) and Wysession *et al.* (1998) also reported a lack of D″ reflections for *P* and *S* waves beneath South Atlantic for some propagation directions and locations.

It is interesting to note that in the low velocity region, close to southwestern Africa, none of the vespagrams (except for one event) show D″ reflected *S* waves despite large direct *S*-wave amplitudes (Fig. 4). Instead, a *P*-reflector is mapped at this location (compare maps of PdP and SdS reflection point locations in Figs 3 and 4). The lack of SdS reflections could suggest the presence of a D″ interface transparent to *S* waves, but able to reflect *P* waves. Causes for this behaviour may be attributed to physical properties of the sampled media, affecting the impedance contrast across this area or perhaps to a distance-azimuthal effect of the SdS reflection coefficient. In previous work (i.e. Pisconti *et al.* 2019), the modelling indeed indicated that certain scenarios of anisotropy lead to a strong reduction of the reflection coefficient along some directions and distances. This behaviour will be considered in the modelling and interpretation of the observations collected in this study as shown below.

Following Thomas *et al.* (2011) and Pisconti *et al.* (2019), we analysed the polarity of the reflected waves. We noted that the lowermost mantle beneath the South Atlantic causes changes in PdP polarity, either the same (positive) or opposite (negative) with respect to main phases PcP or P (see Fig. 3), while the SdS phase always shows the same (positive) polarity as the ScS or S phases (see Fig. 4). The arrows in the figures emphasize the positive (blue arrow) or negative (red arrow) polarity of each wavelet. A similar pattern was also found further to the north, beneath the Central Atlantic (i.e. Pisconti *et al.* 2019). We exclude a source-related cause for the change in the PdP polarity, as demonstrated and discussed by earlier works from Thomas *et al.* (2011) and Pisconti *et al.* (2019). The always positive polarity of the SdS phase is reported by many observations in the literature along with PdP polarity variation (e.g. Thomas *et al.* 2011; Cobden & Thomas 2013; Cobden *et al.* 2015; Pisconti *et al.* 2019; Jackson & Thomas 2021). The occurrence of such behaviour in many studies seems to indicate that this could be a fingerprint of the D″ reflector(s). It has been pointed out by Cobden & Thomas (2013) that an impedance reduction across D″ would lead to a small reflection coefficient for *S* waves, thus resulting in a weak SdS signal with opposite polarity possibly just above the detection threshold that may not be detected. Still, we cannot yet rule out that such a characteristic might pertain to the intrinsic nature of D″ materials.

Modelling and observations shown by Pisconti *et al.* (2019) have underlined the importance of the propagation direction (i.e. in plane or out-of-plane) of the seismic phases for interpreting anisotropy using reflections. This step of the data analysis is particularly important for the interpretation of the PdP polarities for two reasons: (i) complex pattern of PdP-wave polarity depends on the propagation direction and (ii) modelling shows that PdP polarity abruptly changes with azimuth, while SdS exhibits a smoother behaviour, as indeed shown by the data at a global level (see Pisconti *et al.* 2019 or Cobden & Thomas 2013; Cobden *et al.* 2015; Jackson & Thomas 2021, for recent reviews).

To measure the ray direction of the reflected waves, we conducted slowness-backazimuth analysis on all events with PdP and SdS. In contrast to the Central Atlantic study (Pisconti *et al.* 2019), we found that the reflected waves travel mostly in-plane with backazimuth variations less than 5° from the theoretical great circle path (Fig. S1). In some cases, however, the PdP waves display slowness variations up to 0.5–0.6 s deg^{-1} with respect to the PWDK reference model of Weber & Davis (1990), as shown in Fig. S2. These variations may suggest a slight change in the depth of the reflector due to topography or reflections at a tilted interface (e.g. Weber 1993).

Following the approach of previous studies (e.g. Weber & Wicks 1996; Schumacher & Thomas 2016; Schumacher *et al.* 2018; Pisconti *et al.* 2019), to find the depth of the reflector we used a ray tracer and we back-projected the reflections to their most likely bounce points location, provided by the measured slowness, backazimuth, and traveltimesXXX. As expected, the reflection points lie very close to the great circle paths (Fig. 3) but at different depths due to the slowness variation (Table S3). Analysing the depth of the PdP reflection points, we found an average depth of 2730 ± 70 km (∼170 km above the CMB) for PdP waves reflecting outside the LLSVP and a slightly shallower reflection depth within the African LLSVP with an average depth of 2660 ± 100 km (∼240 km above the CMB). The high standard deviation of the latter is due to the high variability of the data, with shallower depths (i.e. 2522 km) at the centre of the LLSVP. Although the values overlap within their standard deviations, the smooth change indicates that the D″ discontinuity shallows inside the LLSVP. However, the scarcity of data and the reduced capability of this methodology to infer topography compared with detailed waveform studies (e.g. Wen 2002) precludes further interpretation of these observations. Overall, our estimations place the D″ reflector in the South Atlantic slightly deeper in the mantle than the previous localized findings of Rost & Revenaugh (2003).

The SdS observations show very small slowness variation with respect to the standard PWDK model of Weber & Davis (1990) and negligible backazimuth deviation from the great circle path (see Fig. S3). Furthermore, given the quasi absence of SdS reflections within the LLSVP (we found only one reflection datum), we cannot compare inside versus outside the LLSVP with the available data. However, previous detailed waveform analysis performed on the *S* waves by Wen (2002) indicate a steep sided edge with elevated topography (∼300 km) near the LLSVP border.

To summarize: firstly, the PdP waves reflecting along the border and outside of the LLSVP show polarity changes, while reflections inside the LLSVP do not experience such polarity changes. Secondly, the SdS waves only show polarities that are the same as the *S* and ScS waves, in the area outside the LLSVP, and do not reveal a reflector inside the LLSVP, except for one single observation

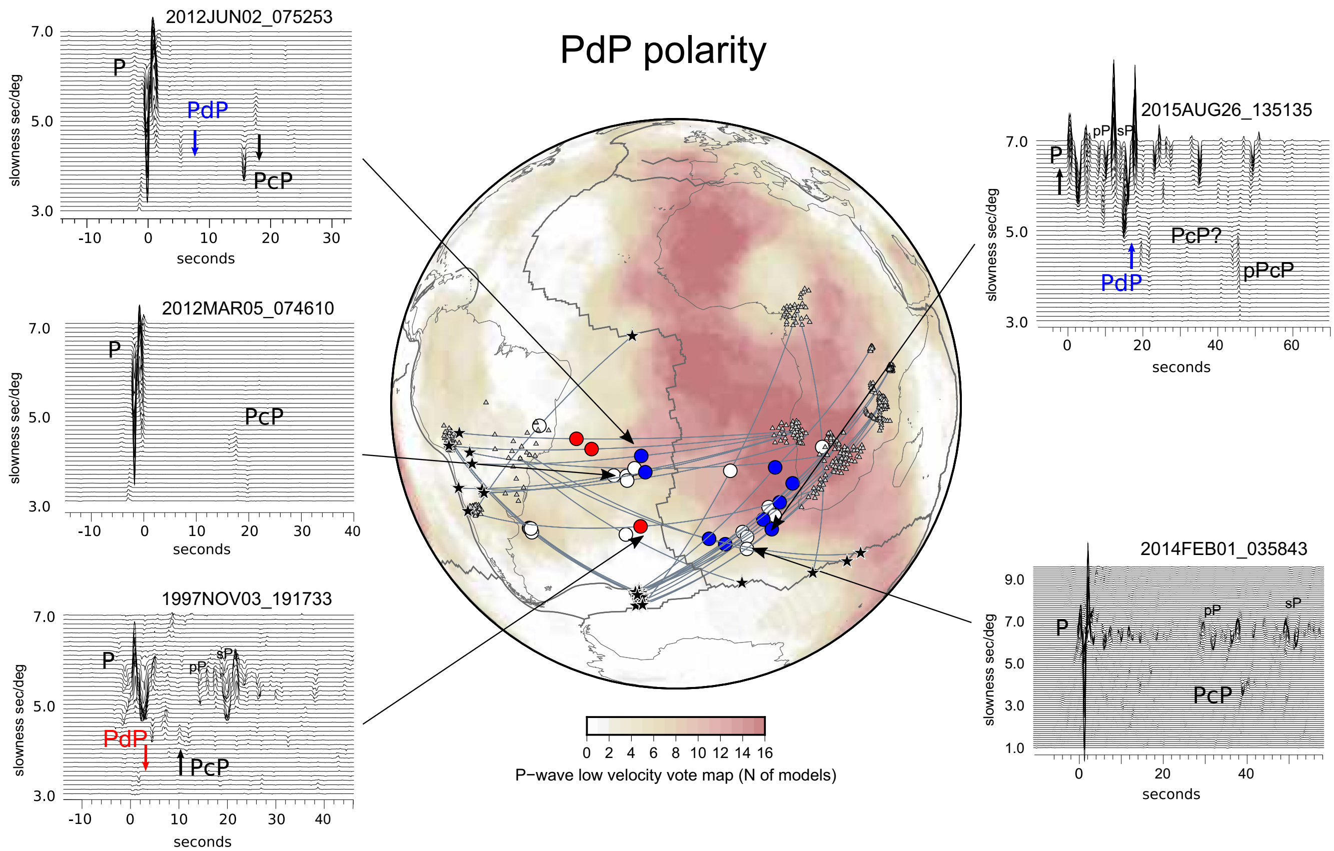

Figure 3. Vespagrams showing some of the collected PdP observations and non-observations in the studied area. Blue (or red) arrows in the vespagrams indicate PdP with same (or opposite) polarity with respect to P and/or PcP. The map at the centre of the figure shows the PdP bounce point locations (blue and red circles), together with the source (black stars) and receiver (grey triangles) configurations. Blue circles indicate positive PdP polarity, red circles indicate negative PdP polarity, while white circles indicate non-observations. The background vote map for *P*-wave low velocity anomaly is computed using tomographic models incorporated in SubMachine (Shephard *et al.* 2017; Hosseini *et al.* 2018).

showing a weak and slightly unclear signal with slowness and traveltime expected for an SdS arrival (Fig. 4, top right). This event samples the LLSVP and shows high amplitude ScS waves which are delayed by ∼10 s with respect to the PWDK reference model (Weber & Davis 1990), indicating a low velocity within the D″ region.

As in our previous studies (Thomas *et al.* 2011; Pisconti *et al.* 2019; Creasy *et al.* 2021), the PdP polarity change is interpreted in terms of reflections with different incidence angles and propagations directions atop of an anisotropic D″ interface. Nevertheless, changes in PdP polarity could also be due to the sampling of a locally varying D″ region in a heterogeneous lowermost mantle. To search for anisotropy in the D″ region that can cause this polarity change, we additionally measured splitting of ScS waves traversing the D″ region.

3.2 Observation of shear waves splitting

Estimation of lowermost mantle anisotropy based on shear waves splitting measurements requires correction for upper mantle anisotropy, which can be performed by differential splitting measurements using a variety of seismic phases such as S, ScS, SKS and SKKS (e.g. Long & Silver 2009; Nowacki *et al.* 2011; Romanowicz & Wenk 2017, for reviews). In this study, we performed S-ScS differential splitting measurements (e.g. Wookey *et al.* 2005) to estimate lowermost mantle anisotropy in the relevant distance range (see Fig. 2a), while correcting for the source side (using *S* waves) and the receiver side [using SK(K)S waves]. Splitting measurements on the *S* and ScS waves, and upper mantle corrections, were conducted using SHEBA (Shear-wave Birefringence Analysis; Wüstefeld *et al.* 2010), which implements the minimum eigenvalue technique (Silver & Chan 1991) on multiple time windows (Teanby *et al.* 2004). All splitting measurements were performed on zero-phase filtered traces using a Butterworth bandpass filter with corner periods of 3 and 25 s.

The correction for the upper mantle beneath the receivers was conducted by taking previously published SK(K)S splitting from the IRIS database (https://ds.iris.edu/spud/swsmeasurement). It is worth noting that for an array deployed in Namibia, no SK(K)S receiver side splitting is available or published as of today. The available upper mantle shear wave splitting measurements across southern Africa (Fig. S4) are very consistent in terms of fast polarization directions, oriented SW–NE. Only one splitting measurement for a station located in Namibia has been published (station TSUM), which also shows a SW–NE trending fast polarization with small delay time (0.42 s), as found by Barruol & Ben Ismail (2001). The authors reported the occurrence of many nulls, as later confirmed by Lynner & Long (2014) who invoked an apparent isotropic upper mantle beneath this station. A small splitting delay time in the upper mantle would have a negligible effect on the ScS splitting estimation which has delay time averaging in the range 1-3 s (e.g.

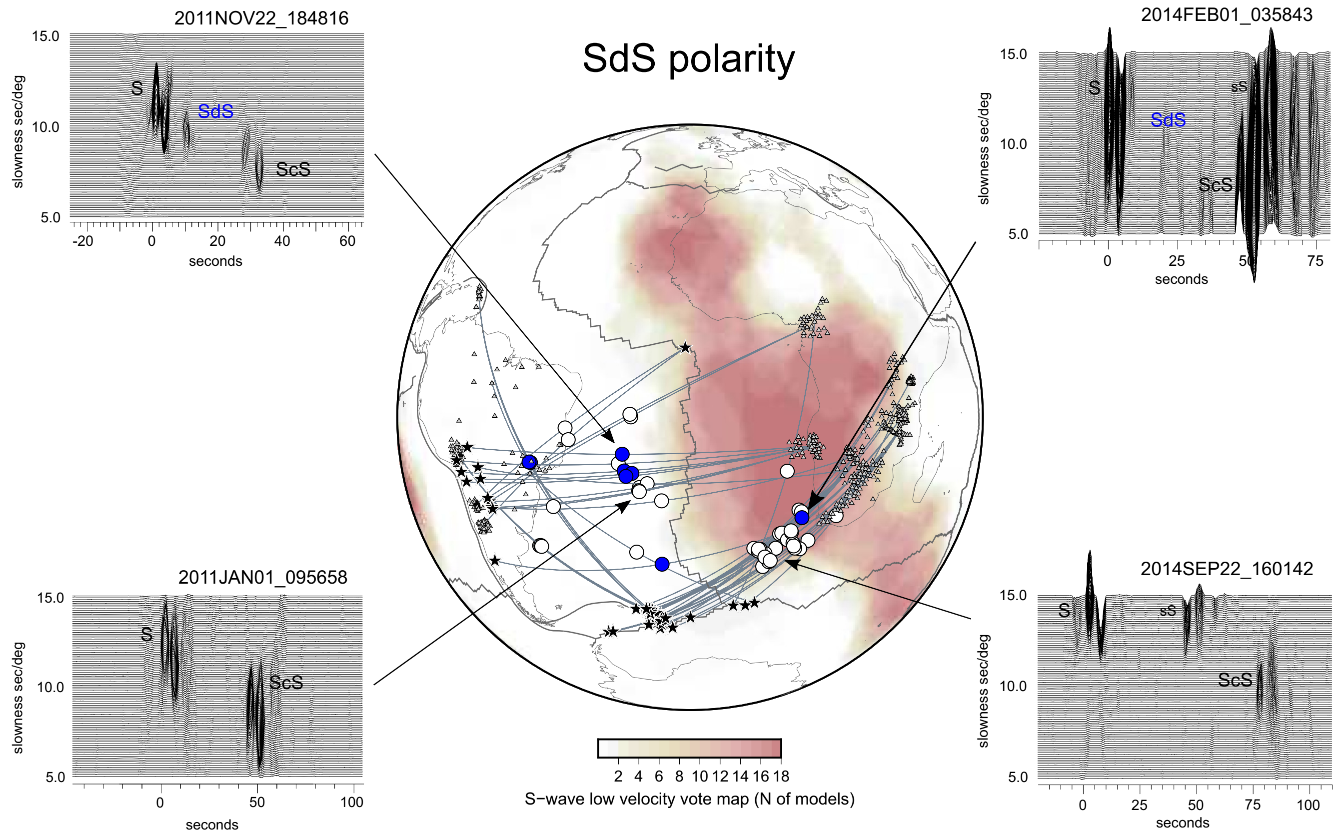

Figure 4. As Fig. 3 but for SdS reflections.

Wookey *et al.* 2005; Ford *et al.* 2015; Nowacki & Wookey 2016; Creasy *et al.* 2017; Pisconti *et al.* 2019; Wolf *et al.* 2019). Given the consistency of the SK(K)S splitting measurements across southern Africa, we assume similar shear wave splitting and upper mantle anisotropy also beneath the array in Namibia. Thus, we consider station TSUM as representative for the splitting at all the stations of the array in Namibia (see Fig. S4) and, given the small delay time, the upper mantle contamination on the ScS waves should not be significant. Based on this assumption, we used the waveforms recorded across the Namibia array for ScS anisotropy estimation in the study region (see left panel of Fig. 5).

We evaluated source side anisotropy in the slab regions from direct *S* waves splitting on a total of 83 good quality event-station pairs. In the Supporting Information, we show typical diagnostic plots for two examples of *S* wave splitting measurements corrected for receiver side anisotropy (Figs S5a and S6a). In Fig. S4 and Table S5, we show the results of the *S*-wave splitting analysis in terms of fast polarization directions back-projected to the source, according to previous work (e.g. Nowacki *et al.* 2010, 2015; Pisconti *et al.* 2019; Wolf *et al.* 2019), along with receiver side corrections from the IRIS database.

The measured source side fast polarizations agree with previous estimates along the subduction zones beneath South America (Lynner & Long 2015; Nowacki *et al.* 2015) and South Sandwich Islands (Lynner & Long 2013). In general, shear wave splitting directions beneath South America are oriented trench-parallel to trench-normal, as also reported in literature (e.g. Lynner & Long 2015). This complex behaviour beneath the South America subduction zone has been related to azimuthal and/or laterally variable anisotropy (Lynner & Long 2015), and to highly anisotropic hydrous phases within slabs (Nowacki *et al.* 2015). The splitting directions observed beneath the South Sandwich Islands are consistent with measurements reported by Lynner & Long (2013) who explain such a pattern with invoking a sub-slab flow, driven by the migration of the Scotia trench along the strike.

With the available upper mantle receiver and source corrections, we carried out splitting measurements on the ScS phases (i.e. the S-ScS differential splitting method of Wookey *et al.* 2005). In total, we collected 44 ScS splitting measurements across a wide area of the lowermost mantle from South America to the southwestern coasts of Africa. Reflection points of ScS waves at CMB and splitting parameters are shown in Fig. 5 and Table S5, respectively. Note that the fast polarizations are projected into the ray reference frame (i.e. following Nowacki *et al.* 2010; Pisconti *et al.* 2019; Reiss *et al.* 2019; Wolf *et al.* 2019).

In Fig. 5, we show two examples of ScS waves experiencing different degree of splitting when traversing the CMB region outside and inside the African LLSVP. Two main characteristics are evident when comparing these waveforms: (i) the late arrival of the ScS wave, sampling the LLSVP, with respect to 1D Earth model prediction (iasp91, Kennett & Engdahl 1991); (ii) the splitting delay time reduction from about 2 seconds (outside) to 1 second (inside) when crossing the border of the LLSVP. These observations suggest a reduction of splitting delay time when sampling the low velocity region beneath Africa. Further examples of ScS splitting estimates and diagnostic plots are shown in Figs S5b and S6b.

In general, we found a horizontal to oblique fast polarization direction in the region outside the LLSVP and a mixture of vertical to oblique fast polarizations inside the LLSVP (Fig. 5). Complex pattern of fast directions changing over small distances were also

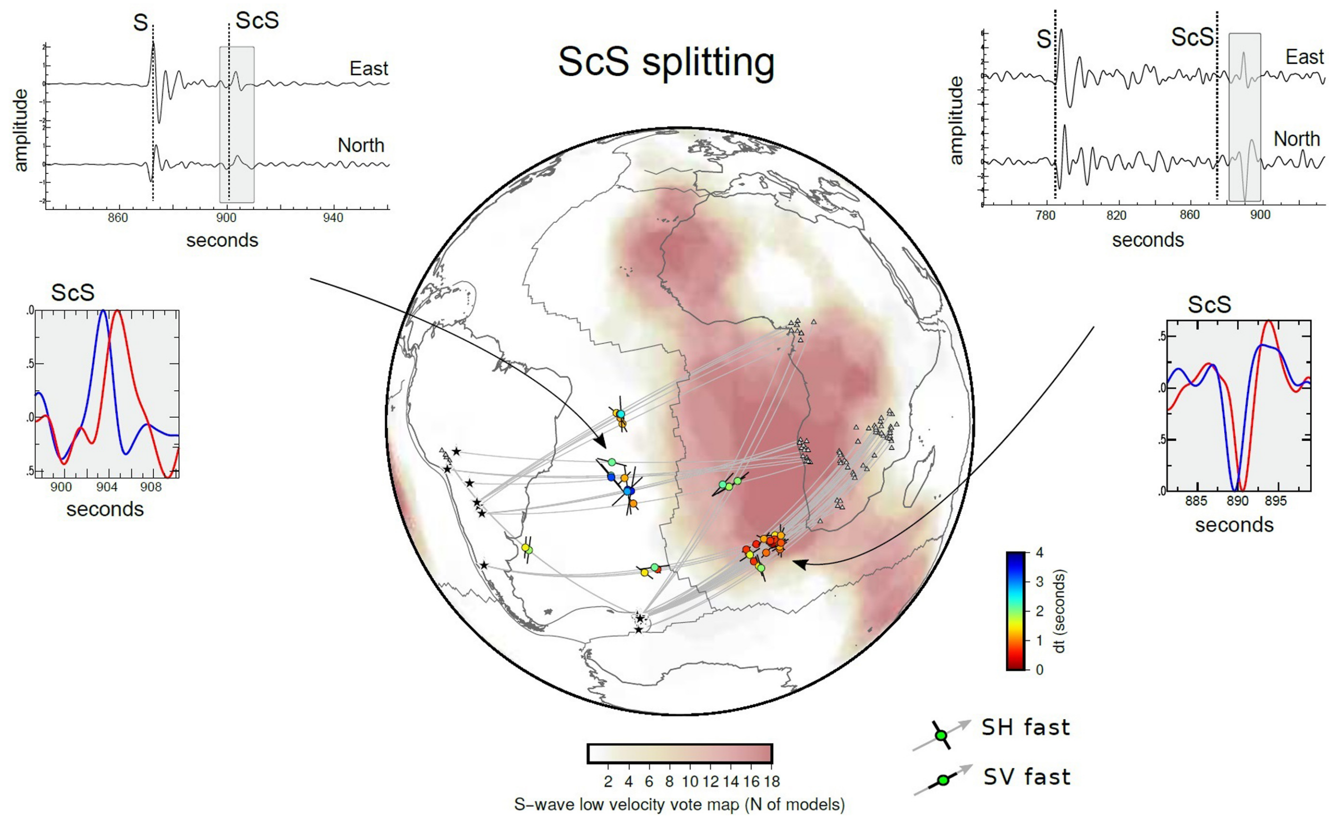

Figure 5. ScS shear wave splitting observations for two events targeting areas outside (left panel) and inside (right panel) the LLSVP. Left panel is for event 2011Nov22_1848 recorded in Namibia (station WP07). Right panel is for event 2008APR14_0945 recorded at the Africa Array (station KTWE). Shown are the horizontal components and the selected time window for the splitting analysis (grey boxes) centred around the ScS waves. Theoretical marks (vertical dashed lines) for the *S* and ScS waves are shown according to the iasp91 model (Kennett & Engdahl 1991). Fast (blue) and slow (red) components are also shown, indicating a smaller splitting delay time for ScS sampling inside the LLSVP. The map at the centre of the figure shows the fast polarization directions, in the ray reference frame, displayed at the ScS bounce points location for the source (black stars) receiver combinations (triangles). When the fast polarization is SV (or SH), the black bar lies along (or perpendicular to) the raypath; in other cases, the fast polarization is oblique. ScS bounce point locations are colour-coded with respect to the splitting delay time. Background vote map as in Fig. 1.

found by Wang & Wen (2007b) and in other areas in the vicinity of the LLSVP border (e.g. Ford *et al.* 2015; Lynner & Long 2015). The ScS splitting delay times, within the LLSVP and across its border, observed in our study also agrees with observations on the eastern and southern border of the African LLSVP and interpreted as reduction in anisotropy strength within the African LLSVP (Cottaar & Romanowicz 2013; Ford *et al.* 2015; Lynner & Long 2015). Splitting delay times of 1 s on the SKS-SKKS phases were also measured by Wang & Wen (2007b) inside the LLSVP.

The splitting measurements for shear waves sampling the regions outside the African LLSVP provide new results of D″ anisotropy in this part of the Earth which was not explored before (see Creasy *et al.* 2019 for a recently updated map of D″ splitting studies). Overall, the observation of splitting in the D″ region beneath the South Atlantic strengthens the hypothesis that the variation in the PdP polarity might be caused by anisotropic reflections. These results agree with our previous findings (Pisconti *et al.* 2019) over a contiguous D″ area, further to the North beneath the Central Atlantic.

Some caveats exist with some of the assumptions we make when interpreting splitting in the D″ region. Synthetic modelling studies (e.g. Maupin 1994; Komatitsch *et al.* 2010; Borgeaud *et al.* 2016; Parisi *et al.* 2018) have shown that, for phases that sample the lowermost mantle, apparent shear wave splitting can arise in isotropic media in certain circumstances, due to finite frequency effects. However, these studies have mainly focused on larger distances (>85°) and on different seismic phases (*S* and S_{diff}) than those used here (ScS at 50–80°). Specifically designed waveform modelling tests on ScS wide-angle reflections, in the relevant distance range, were performed by Nowacki & Wookey (2016). These authors showed that isotropic models do not produce ScS apparent splitting, validating the S-ScS differential splitting method of Wookey *et al.* (2005) used here, as later discussed by Wolf *et al.* (2019). Very recently, Wolf *et al.* (2022a,b) looked at non-ray-theoretical effects on splitting due to lowermost mantle anisotropy and at the effect of corrections for upper mantle anisotropy contributions. These studies showed that ScS/S and SK(K)S phases can be used to measure splitting in D″ in many or most circumstances (although with some caveats related to the initial polarization of the ScS phases and the strength of upper mantle anisotropy; see Wolf *et al.* 2022b), and that the interpretation in terms of D″ anisotropy is in general reliable for stations with weak receiver side upper mantle anisotropy, as in this study.

4 MODELLING AND RESULTS

We model our observations following the procedure developed and outlined in our previous studies (e.g. Creasy *et al.* 2019, 2021; Pisconti *et al.* 2019). The reader is referred to those studies for more details, and here we only give a concise review, since this work represents a further advancement of our previous studies. Both Lattice Preferred Orientation (LPO) and Shape Preferred Orientation (SPO) scenarios are considered as possible causes for anisotropy in the study region (e.g. Nowacki *et al.* 2011). Elastic constants and densities for single crystals and fabrics of D″ mineralogical phases, such as bridgmanite (bm), post-perovskite (ppv), MgO, including different slip systems, were taken from previous studies (Ford *et al.* 2015; Goryaeva *et al.* 2015, 2016; Karki *et al.* 1999; Yamazaki *et al.* 2006; Mainprice *et al.* 2008; Walte *et al.* 2009; Miyagi *et al.* 2010; Thomas *et al.* 2011; Wu *et al.* 2017; Tommasi *et al.* 2018). Following Thomas *et al.* (2011), in these anisotropic models the slip direction is assumed to be parallel to the imposed deformation direction. We also tested aligned tubular/oblate-shaped melt pockets in SPO fabric (e.g. Kendall & Silver 1996, 1998; Nowacki *et al.* 2011; Ford *et al.* 2015). Elastic constants for all tested cases are reported in Table S6.

Following Creasy *et al.* (2019; 2021), Pisconti *et al.* (2019) and Thomas *et al.* (2011), in our models we assumed an isotropic lower mantle over an anisotropic D″ region, separated by a horizontal flat and sharp discontinuity. It can be argued that these assumptions are too simplistic with respect to real Earth complexity. In principle, seismic anisotropy could be anywhere in the lower mantle below the turning depth of *S*. As the ScS and *S* waves travel different paths, particularly for short epicentral distances, splitting acquired along the paths of *S* and ScS could differ. The presence of significant anisotropy in the lower mantle just above the D″ region would imply the modelling of a two-layers anisotropic model. Such a scenario would change the reflection coefficients, as shown for the wadsleyite-olivine phase transition in mantle transition zone studies (Saki *et al.* 2018). Future investigations will need to explore more complex and perhaps more realistic settings.

As of today, there is no clear evidence and consensus on significant anisotropy in the bulk of the lower mantle above D″ away from the subduction zones (see Romanowicz & Wenk 2017, and references therein for a review) and mechanisms of deformation acting in the lower mantle may not lead to observable anisotropy (Karato & Li 1992; Karato *et al.* 1995; Meade *et al.* 1995; Karato 1998a, b; Kendall 2000). Other studies have also consistently argued that on a global scale, seismic anisotropy is present in the D″ layer, but generally not in the bulk of the lower mantle, based on different types of observations (e.g. using normal modes: Moulik & Ekström 2014; using body waves: Meade *et al.* 1995; Usui *et al.* 2008; see Romanowicz & Wenk 2017, for a recent review).

The hypothesis of an isotropic lower mantle was also tested by Pisconti *et al.* (2019), who performed SdS splitting measurements at single stations and found that the SdS phase displays roughly the same splitting parameters as the *S* wave that bottoms in the lower mantle above D″. *S* and SdS both display much smaller splitting delay time than the ScS wave, which propagates within the D″ region. This observation indeed suggests negligible anisotropy in the lower mantle in the few hundreds of km just above the D″ beneath the nearby region of the Central Atlantic, and that the larger ScS splitting is accumulated within the D″ region rather than just above it. Unfortunately, the SdS splitting analysis performed by Pisconti *et al.* (2019) is not usually feasible using single stations due to noise and the consequent difficulty in picking such a weak arrival; the SdS phase is usually detected with array processing (e.g. Rost & Thomas 2002). Additionally, the subset of waveforms for the present study relevant to the short distances, where the *S*- and ScS-wave paths in the lower mantle differ, show only a weak stacked SdS signal (Fig. 4), preventing us from performing SdS splitting analysis in this work. Because of this limitation, we rely on previous constraints on lower mantle anisotropy to assume that in our study region the anisotropy is mostly confined in the D″ reflecting layer, as also assumed by many other studies (e.g. Wookey & Kendall 2008; Nowacki *et al.* 2010; Ford *et al.* 2015; Creasy *et al.* 2017; Pisconti *et al.* 2019; Wolf *et al.* 2019).

While we use a horizontal flat and sharp discontinuity, topography of the D″ reflector is documented in the literature (e.g. Thomas *et al.* 2004a, b) and should be considered when interpreting seismic phases bouncing off these structures. We have not yet found that topography of the D″ discontinuity causes polarity reversals in D″ reflected waves; however, if topography of the D″ discontinuity were rough enough to cause polarity changes, it would likely also change the propagation direction (i.e. significantly changing the slowness and backazimuth of the waves, and thus the traveltime). We do not find such large variation in our measurements (Figs S1, S2 and S3) with respect to a standard 1-D model (i.e. PWDK, Weber & Davis 1990), implying that topography, if present, would be smooth, at least in the studied areas. As in Thomas *et al.* (2011) and Pisconti *et al.* (2019), we assume a sharp D″ discontinuity considering that an effective interface thickness as sharp as 40 km could be inferred from our observations and their frequency content (for a 6 s SdS reflection and for a 3 s PdP reflection).

Using these assumptions, we calculated PdP and SdS reflection coefficients and ScS splitting parameters for all distances between 50° and 80° and azimuths between 0° and 360°. Incidence angles on top of D″ discontinuity and CMB were computed using the Taup Toolkit (Crotwell *et al.* 1999). Reflection coefficients and splitting parameters were computed following Guest *et al.* (1993) and Walker & Wookey (2012), as described in Pisconti *et al.* (2019). As performed in previous studies (e.g. Nowacki & Wookey 2016; Pisconti *et al.* 2019), in our ScS splitting predictions we consider the effect of the ScS incidence angle (i.e. epicentral distance) and the different splitting operator for the incident and reflected ScS legs, on either side of the core reflection point. The accuracy of this modelling approach has been recently investigated using global full wavefield simulations by Wolf *et al.* (2022b), who found that this style of ray-theoretical predictions is in general more accurate than those that assume a horizontal ScS propagation through D″.

As in our previous work (i.e. Pisconti *et al.* 2019), we rotated all our models in all possible directions and retained only those models which predict at least 68 per cent of each type of observations (i.e. PdP, SdS polarity and ScS splitting). Further details concerning the fitting procedure and the potential constraints on the models gained by the joint use of reflections and splitting are found in Pisconti *et al.* (2019). In this work we extended this approach to test regional/lateral variation in anisotropy, mineralogy, and deformation across the studied area based on the geographical distribution and pattern shown by our data, therefore more emphasis is given to this aspect as it follows.

The overall geographical distribution of PdP, SdS and ScS reflection points (Fig. 6) covers a large area of the D″ region beneath the South Atlantic despite the gaps in data coverage. Considering the location of the African LLSVP and its border beneath the South Atlantic, we subdivided these measurements in three subregions:

(i) *region 0* pertains to D″ areas located far from the LLSVP, that is beneath South America. It contains few measurements (SdS polarity and ScS splitting) and zero PdP polarity observations (see Figs 3–5).

(ii) *region 1* contains measurements located in the vicinity of the LLSVP border beneath the South Atlantic Ocean, and it represents

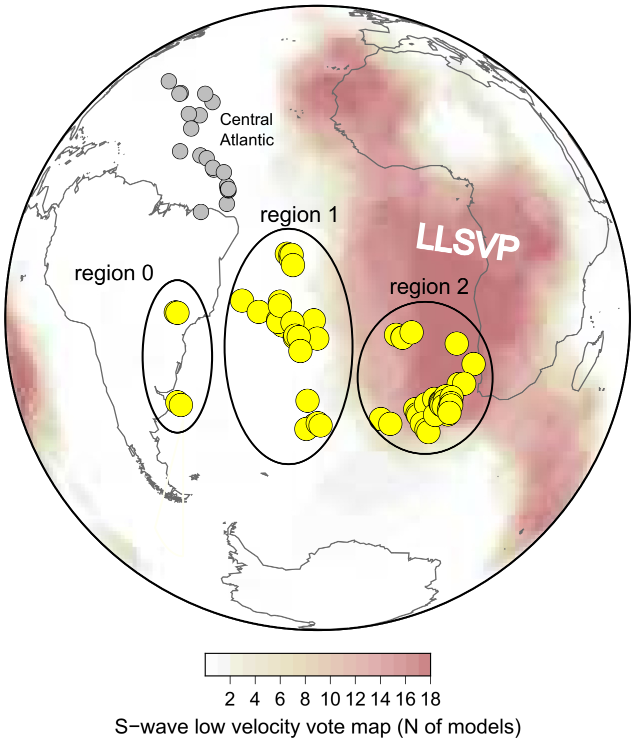

Figure 6. Geographical distribution of the bounce points (yellow circles) for PdP, SdS and ScS waves collected in this study. Three subregions can be identified, based on their location with respect to the LLSVP (see text). Background vote map as in Fig. 1. Grey circles indicate reflection points beneath the nearby region of the Central Atlantic (i.e. Pisconti *et al.* 2019) as described in the text.

a collection of both PdP, SdS polarities and ScS splitting. In this region, the PdP reflected waves exhibit changes in polarity, in analogy to the contiguous Central Atlantic region previously investigated by Pisconti *et al.* (2019) for which *region 1* might be considered as a continuum further to the south.

(iii) *region 2* groups observations falling within the LLSVP, indicating a smaller amount of anisotropy (smaller splitting delay times) compared to *region 1*, no PdP polarity changes and a seemingly transparent D″ discontinuity to shear waves.

This geographical subdivision of the measurements is merely based on the available coverage and gaps, which could bias the interpretation when modelling these observations separately, in the sense that the geographical distribution might not reflect the actual Earth complexity. Therefore, in the modelling of the observations, we also considered all possible combinations of the subregions: that is *region 0-1 (i.e. region 0 + region 1)*, *region 1-2 (i.e. region 1 + region 2)* and *region 0-1-2*, the latter includes all the measurements together. In principle, if a model can reproduce all the measurements as an ensemble (i.e. *region 0-1-2*), that model could be taken as the most likely scenario since is the simplest explanation for the data variability over a large area. This case would imply a homogeneous (although anisotropic) medium for the D″ beneath the South Atlantic, from South America to Africa and traversing the LLSVP border. We tested this hypothesis as starting point in the modelling.

Starting from the simplest scenario of homogeneous anisotropy across the entire area (i.e. *region 0-1-2*), we found that none of the models (explanation of cases in Fig. 7a) can adequately explain all of the data (see Fig. 7b), therefore a lateral variation in anisotropy must be invoked to account for the data variability. The best-fitting model, case A, can reproduce the measurements of sub-*region 2* within the LLSVP, but it fails to predict the PdP negative polarity in sub-*region 1*, as shown in the pole figures of anisotropy in Fig. 7(c). The same result is also true for the other models, such as case B and C, where the PdP polarity variation cannot be reproduced. As for the Central Atlantic (Pisconti *et al.* 2019), the PdP-wave polarity provides a strong constraint on the plausible style and mechanism of anisotropy, which is otherwise not achievable with shear waves splitting alone. The inability of all models to reproduce the observations covering such a large area traversing the LLSVP border suggests that the hypothesis that anisotropy is homogeneous in D″ does not hold. Therefore, in a next step, we opted for a division of the measurements in two subregions, that are (i) *region 0* with *region 1-2* and (ii) *region 0-1* with *region 2*.

Region 0 is unconstrained by the available data because there are too few data to narrow down the number of plausible models (on the order of 10^5) for a feasible interpretation. Moreover, no PdP reflection data were found beneath South America, which would help restricting the possible cases, as mentioned above. On the other hand, the results for *region 1-2* across and within the LLSVP border are essentially the same as *region 0-1-2*, because *region 0* does not help with constraining a given model. Shear planes and directions for the *region 1-2* are shown in the Fig. S7, for a comparison with Fig. 7.

Region 0-1 provides the best example of constraining the anisotropy using a combination of reflections and splitting measurements. Indeed, there is only one case (i.e. case E), with few rotation combinations, that fit the observations while predicting the variation in PdP polarity (Fig. 8a). Pole figures for anisotropy for *region 0-1* are shown in the Fig. 8(b). In contrast, *region 2* (Fig. 9a) is not well constrained by the available observations as *region 0-1*. This might be a result of the limited spread in both azimuth and distance but also by the consistent positive PdP polarity and only one SdS observation. *Region 0-1* and *region 2* represent then two extreme cases for our methodology with advantages and disadvantages due to a good and poor azimuthal coverage, respectively.

When considering the best-fitting model for *region 2*, case A, it is worth mentioning that this scenario is very effective in reproducing the lack of SdS observations, as illustrated in the pole figures of anisotropy in Fig. 9(b). Along these directions, the model predicts very low SdS reflection coefficient, thus explaining the apparent absence of a D″ reflection in the *S* waves, while still reflecting the *P* waves without any polarity change across the azimuths. At very large distances this reflector seems to appear in the *S* waves (1 datum, see pole figures in Fig. 9b and the relevant vespagram in Fig. 4, top right-hand panel). Furthermore, the best-fitting model also reproduces very small ScS splitting delay time and varying fast polarization directions, as found in our data for *region 2* (Fig. 9b) within the LLSVP.

The observations for *region 2* seem to be incompatible with the presence of a mineralogical phase transition from bm to ppv within the LLSVP but can be explained invoking a change in fabric from isotropic to LPO texture in bm. The alignment of bm may result from a topotactic transformation, where LPO in ppv is inherited into the bm stability field (e.g. Walker *et al.* 2018). The best-fitting model for *region 2* is also able to predict smaller splitting delay times within the LLSVP, compared with *region 0-1* outside the LLSVP.

In a last step we tested each sub-region separately. As already explained above, *region 0* is unconstrained and *region 2* can be represented by a set of rotations of case A. This leaves *region 1* to be tested, separately. From Fig. S8, we note that *region 1* is well constrained. However, when adding the few measurements from

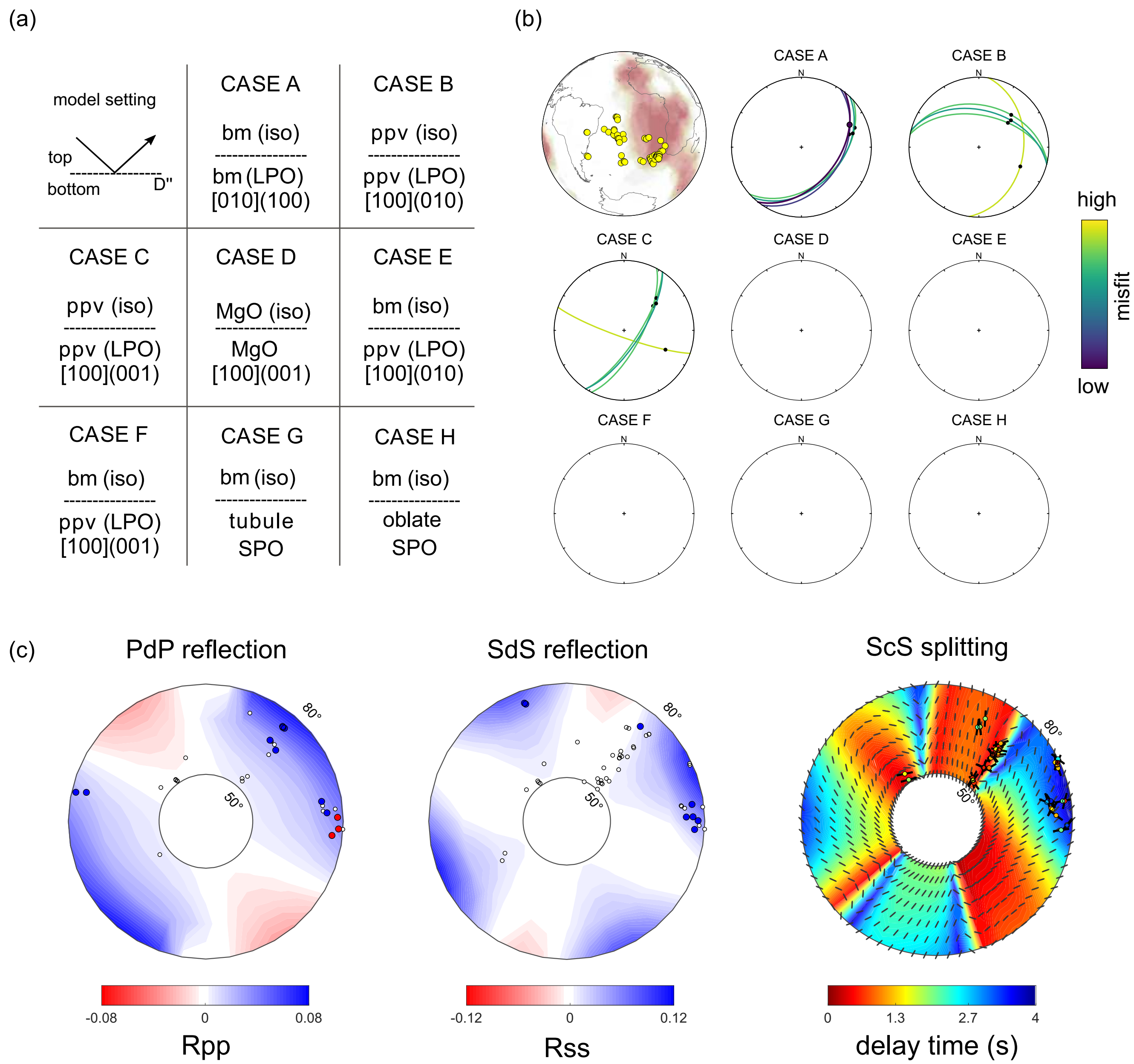

Figure 7. (a) Settings of the different cases tested in this study with elastic constants and densities as shown in Table S6. Top left-hand panel: schematic illustration of a reflection from the D″ discontinuity. Cases A to D, LPO with only texture change and no phase transformation. Cases E and F, LPO with phase transformation. Case G and H, SPO with tubule and oblate melt pockets. (b) Stereonets (upper hemisphere projection) showing shear planes (great circles) and directions (black points), for the rotated cases, colour-coded with respect to the misfit (i.e. number of fitted observations, low misfit-high number), for *region 0-1-2*. (c) Pole figures of anisotropy in terms of reflection coefficient and splitting for the best-fitting model for *region 0-1-2*. The model corresponds to case A, with deformation direction rotated by 65° from north and a tilted shear plane dipping 25°. Solid points on the pole figures indicate the observed reflections (i.e. polarities) and the black bars indicate the splitting observations (i.e. fast polarizations) with colour-coded delay time. Note the incapability of this model to reproduce the negative PdP polarity observations (red points). Blue points represent positive PdP and SdS polarity observations, whilst white points represent non-observations.

region 0 (i.e. *region 0-1*, Fig. 8), extending the region outside the LLSVP towards South America, both data sets are well represented by a common model which tends towards a unique solution, that is case E (compare Figs 8 and S8). This model reproduces more observations (lower misfit) over a larger area compared with two different models for *regions 0* and *1*. It also compensates for the lack of constraints on *region 0*. For the sake of simplicity, we favour a common model as it reproduces more measurements and can plausibly explain both data sets.

The results presented above highlight the capability of the combined approach of using reflections together with splitting in constraining and narrowing down possible models. It is noteworthy that D″ reflection and splitting observations are complementary in tightly constraining a given scenario of anisotropy, deformation, and mineralogy (Pisconti *et al.* 2019). This explains the well constrained scenario for the region outside the LLSVP (Fig. 8), despite the comparatively small number of observations. This approach was in addition quantitively assessed in a synthetic test

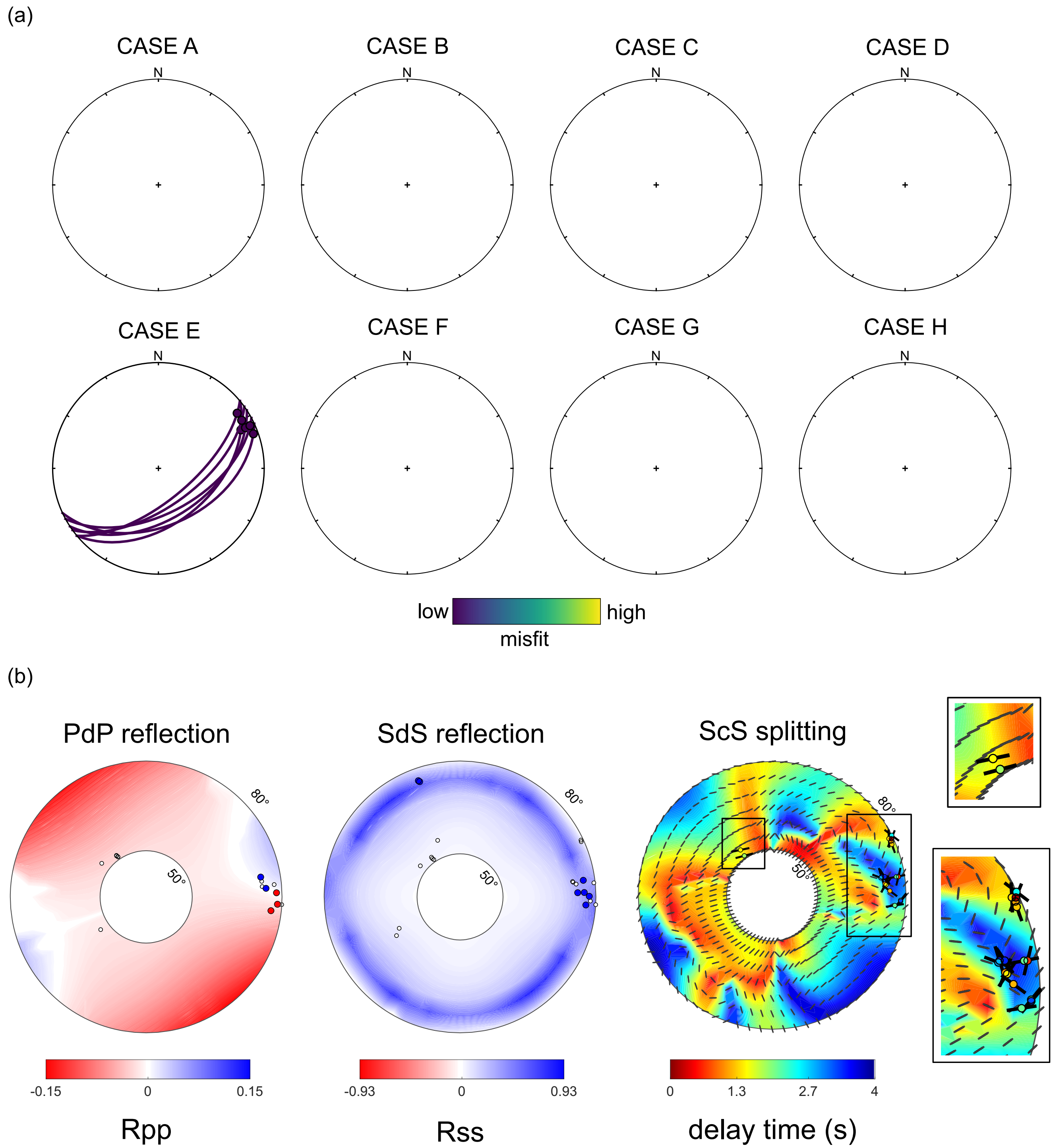

Figure 8. (a) Stereonets showing shear planes and directions for *region 0-1*. (b) Pole figures of anisotropy for the best-fitting model for *region 0-1*. The model corresponds to case E with deformation direction rotated by 60° from north and a tilted shear plane dipping 10°.

(Creasy *et al.* 2019), who found that by adding only one reflection polarity datum to a small data set of 6–7 splitting measurements, the probability of uniquely recovering a starting model increases by about 15–20 per cent. In that study, they also analyzed the effect of the azimuthal distribution of the ray paths on the probability to constrain a given starting model, finding that this dependency has only a weak effect. These findings suggest that the combination of different types of measurements (i.e. different methods and wave types) is more efficient in recovering anisotropy than a multi-azimuthal sampling but with only one type of measurement (i.e. splitting). These synthetic results are supported by real data sampling the D″ region beneath the Central Atlantic (Pisconti *et al.* 2019) and Siberia (Creasy *et al.* 2021).

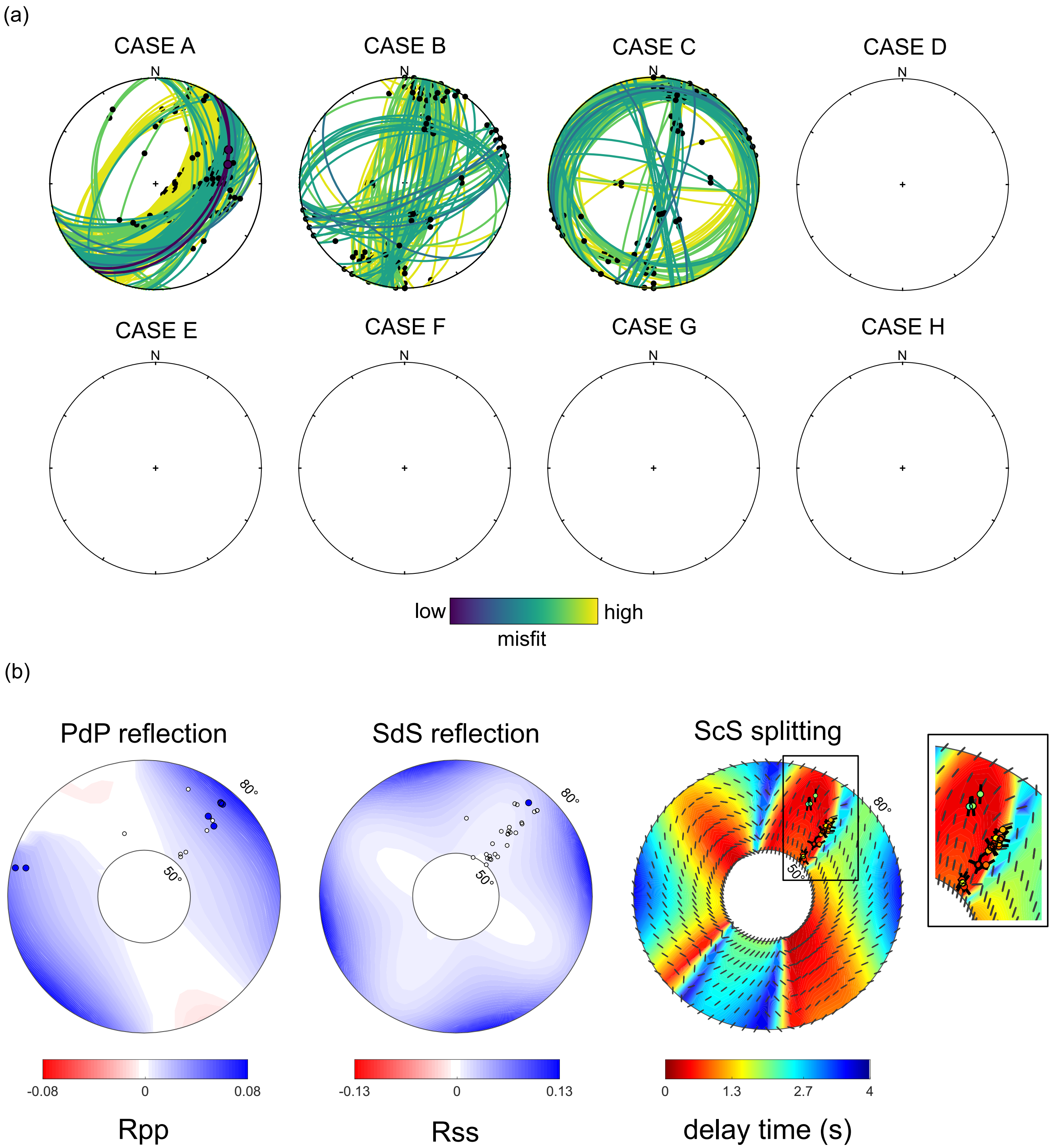

Figure 9. (a) Stereonets showing shear planes and directions for *region 2*. (b) Pole figures of anisotropy for the best-fitting model for *region 2*. The model corresponds to case A with deformation direction rotated by 75° from north and a tilted shear plane dipping 30°.

5 DISCUSSION

Modelling of the observations of reflections and splitting in the lowermost mantle beneath the South Atlantic, we identified two plausible distinct scenarios relating to two ensembles of measurements: case E (isotropic bm over aligned ppv) for *region 0-1* and case A (isotropic bm over aligned bm) for *region 2*.

Region 0-1 is large and includes measurements on seismic waves reflecting outside the southwestern border of the African LLSVP. These measurements are compatible with a phase transition from randomly oriented bm to LPO in ppv accommodating deformation along the [100](010) slip system (case E in Fig. 8a). From the family of shear planes and directions, we computed an average deformation direction of 63 ± 5° from north, which points towards the LLSVP (Fig. 10) and is tilted by 9 ± 4° from the horizontal (i.e. CMB). This model, although with a different deformation orientation, was also found in the nearby region of the Central Atlantic, towards to

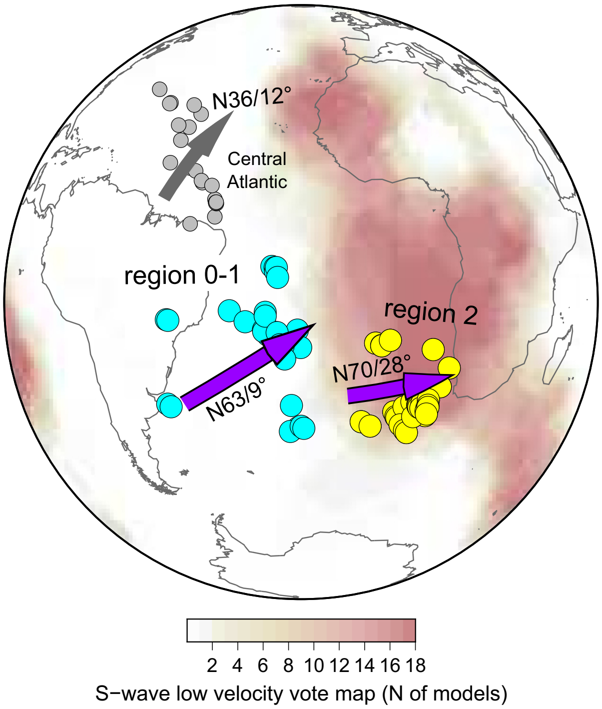

Figure 10. Deformation directions (purple arrows) in the lowermost mantle beneath the South Atlantic, as inferred in this study. Region 0-1 (cyan circles) displays a N63° oriented slip direction tilted by 9° upwards, whilst region 2 displays a N70° oriented slip direction tilted upwards by 28°, both pointing towards the LLSVP. The length of the arrows is approximately scaled with respect to the size of the regions covered by the data sets. The Central Atlantic study from Pisconti *et al.* (2019) (grey circles) is also indicated, with deformation direction N36/12° (grey arrow). Background vote map as in Fig. 1.

the north of the area studied here (see Fig. 10 and Pisconti *et al.* 2019). If a continuous D″ region (and reflector) is assumed across the Central and South Atlantic area, it might suggest the presence of a homogeneous (although anisotropic) deep mantle off the western border of the African LLSVP and dominated by the presence of a bm to aligned ppv [100](010) phase transition with analogous deformation style. However, the geographical gap in our data at subequatorial latitudes needs to be covered in future work to assess whether such a continuity is indeed present.

Ford *et al.* (2015) infer LPO in ppv [100](010) from splitting measurements for a region located at the eastern edge of the African LLSVP. We find that the same slip system for ppv explains the observations in the South Atlantic (i.e. *region 0-1*) and further North in the Central Atlantic in a relatively fast region (i.e. Pisconti *et al.* 2019). Furthermore, slip on the (010) plane also agrees with theoretical calculations on plausible dominant deformation mechanisms for ppv from Goryaeva *et al.* (2016, 2017) and used also by Tommasi *et al.* (2018) to predict seismic anisotropy at the base of the mantle.

Palaeo-subduction reconstructions based on global tomography (van der Meer *et al.* 2018) place an ancient slab beneath the South America—South Atlantic area (across our *region 0-1*). The authors suggest a possible common origin of such a slab (called Sao Francisco slab) with the Atlantis slab located beneath the Central Atlantic and due to the subduction of the Triassic Panthalassa Ocean. This interpretation agrees with the study of Cottaar & Romanowicz (2013), who found ppv within fast seismic velocities in the region outside the southern African LLSVP, off the coast of Antarctica. For such palaeo-subduction regions, Nowacki *et al.* (2013) inferred LPO of ppv, accommodating slip on (010), which agrees with our results for *region 0-1*.

Region 2 includes observations that sample the lowest velocities within the LLSVP, according to the vote map for low shear wave velocity in tomography models (see Fig. 6). Here, the available observations suggest a texture transition from randomly oriented bm to LPO in bm accommodating deformation along the [010](100) slip system (case A of Figs 9a and 7a) which, according to Mainprice *et al.* (2008), would be the easiest glide system. However, the quality of the fitting is weaker than in the other regions and other scenarios might also be possible, such as cases B and C. These cases also correspond to texture changes of ppv with two orthogonal slip (shear) planes, i.e. (010) and (001), respectively. Shear plane orientations of these cases differ by 90°, but the shear (slip) direction remains unaltered. Therefore, with the available results, these two cases can be interchanged without changing mineralogy and deformation direction, but only changing slip plane, as it was also found by Pisconti *et al.* (2019) and Creasy *et al.* (2021).

In search for additional constraints, we compared these best-fitting models with recent SK(K)S splitting measurements from Reiss *et al.* (2019), which partially sample *region 2* at the northernmost border. Using these SK(K)S splitting results, we can rule out case B, as the observed fast polarization directions do not match this scenario, whilst cases A and C, for the relevant rotated cases, still match the observations (Fig. S9). However, since the ray paths for these SK(K)S observations only sample the northernmost borders of *region 2* (inset of Fig. S9), we refrain from placing further constraints based on these measurements. Despite the ambiguity of the results on *region 2* and if we rely on the model with the lowest misfit, case A is our preferred model for this region (Fig. 9a). Using case A, there are two different possible deformation directions with the lowest misfit which average a direction of 70 ± 7° from the North and tilted 28 ± 4° from the horizontal (Fig. 10).

By comparing the inferred deformation directions of *region 0-1* (N63°) and *region 2* (N70°) we note that the deformation slightly changes within the LLSVP (Fig. 10) and, more significantly, increases its vertical component from 9 ± 4° to 28 ± 4° relative to the CMB (as schematically illustrated in the cartoon of Fig. 11). The resulting deformation direction in the South Atlantic and the results of Pisconti *et al.* (2019) agrees with the deep mantle flow pattern predicted by Simmons *et al.* (2009). Deep mantle flow circulation which rotates and is deflected upwards at the LLSVP border might be related to the LLSVP edge acting as a mechanical boundary (Cottaar & Romanowicz 2013; Reiss *et al.* 2019). Cottaar & Romanowicz (2013) also suggested a reduction in the strength of anisotropy in the vicinity and within the LLSVP, which agree with the findings of our study. Indeed, outside the LLSVP (i.e. *region 0-1*), we found an average shear wave anisotropy of 1.6 ± 0.6 per cent due to LPO in ppv (case E), while inside (i.e. *region 2*) it weakens to 0.98 ± 0.14 per cent due the LPO in bm of case A.

Bm-enriched LLSVPs have been proposed in several studies investigating the compositional properties and the possible primitive nature of these regions of the mantle, with iron-bearing bm being most plausible (Deschamps *et al.* 2012; Vilella *et al.* 2021). If the LLSVPs represent hotter regions of the mantle (McNamara 2019), bm is expected to dominate the mineralogical composition rather than ppv, due to the positive Clapeyron slope of the bm-ppv system (Oganov & Ono 2004; Tsuchiya *et al.* 2004; Hernlund *et al.* 2005; Catalli *et al.* 2009), although the stability fields depend on pressure

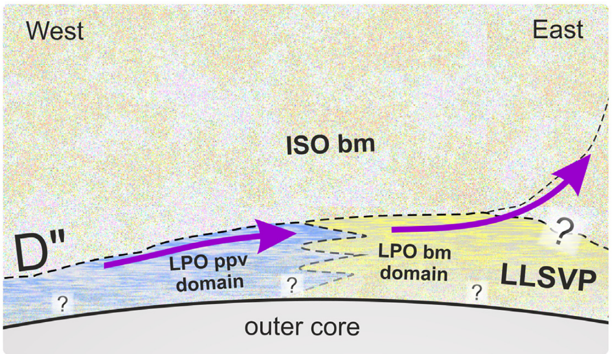

Figure 11. Cross section (roughly W–E) cartoon depicting the most likely scenario of the D″ region beneath the South Atlantic, according to the collected data sets. A thicker D″ layer within the LLSVP is represented as a slightly elevated D″ discontinuity (dashed line), according to our data. Purple arrows indicate deformation direction pointing towards the LLSVP and increasing its vertical component in the vicinity of the LLSVP. LPO of post-perovskite (ppv) and bridgmanite (bm) are expected outside and inside the LLSVP, respectively, whilst an overall randomly oriented bm is present in the lower mantle. The uncertain location of the ppv to bm lateral boundary is illustrated as interlayering between the two domains. Less well-constrained areas within the LLSVP and in the vicinity of the CMB are indicated with shaded colours and question marks.

and on the amount of iron and alumina (e.g. Sun *et al.* 2018; Vilella *et al.* 2021).

An underlying assumption in our models is the vertical uniformity of fabric and mineralogy from the D″ discontinuity to the CMB. It is likely that the LPO changes laterally and in depth in the lowermost mantle due to varying strain field (e.g. McNamara *et al.* 2002). Another hypothesis is the possibility of a back-transformation of ppv to bm in the vicinity of the CMB (e.g. Hernlund *et al.* 2005). In principle, these vertical variations would generate additional seismic signals, as previously proposed for other regions (e.g. Hernlund *et al.* 2005; see Jackson & Thomas 2021, for a review). Texture changes might also contribute to a reflected signal in a similar manner as PdP waves reflect from within the LLSVP in this study. In our analysis, however, we do not find evidence for (or our resolution is not good enough to resolve) a secondary arrival with intermediate slowness and traveltime between PdP/SdS and PcP/ScS. Thus, we do not invoke the presence of an additional structure representing a vertical variation in mineralogy and/or fabric.

In our models, the depth of the bm-ppv phase transition and the onset of the LPO of ppv coincide; however, in the real Earth this may not necessarily be true. If we assume the existence of sharp reflectors, there could be (in principle) two distinct reflected seismic signals occurring in a depth range (i.e. one for the bm-ppv transition and one for the fabric change, similar to the case above). Again, we do not find such additional signals in the stacked vespagrams, which suggests that there is little or no gap in depth between the phase transition and the LPO onset, within the resolution of our analysis (40 km vertically for 6 s SdS and for 3 s PdP). While this simplistic scenario explains the observations, complexities in the D″ region at depth approaching the CMB may still be present (e.g. Jackson & Thomas 2021) and cannot be ruled out in the investigated areas. The non-observation of additional reflections from deeper structures still represents valuable information, however.

Taken together with results from Pisconti *et al.* (2019), our findings indicate the presence of a ppv rich lowermost mantle outside the LLSVP and a bm rich lowermost mantle within the LLSVP. It appears that bm replaces ppv as the major constituent of the lowermost mantle inside the LLSVP, where a different deformation direction is likely to act. Our results agree well with a recent study by Chandler *et al.* (2021), who use geodynamic modelling and atomistic models to predict seismic anisotropy.

The presence of a lateral transition from a ppv domain outside the LLSVP to a bm domain within the LLSVP (Fig. 11) might be due to a temperature increase close to the LLSVP (McNamara 2019). The geographical location of the two subsets of measurements (i.e. *region 0-1* and *region 2*) suggests that the lateral transition from ppv to bm may occur somewhere close to the southwestern border of the LLSVP, across a few hundred km (<800 km) wide zone. Up to now, the geographical location of the LLSVP edges is not well constrained, particularly for the African LLSVP and it is not clear yet whether these sharp edges are thermal or thermochemical boundaries, (see Hernlund & McNamara 2015; Garnero *et al.* 2016; McNamara 2019, for recent reviews). Locating these borders is crucial for our understanding of the dynamics and evolution of the LLSVPs (see Ni & Helmberger 2003b; Torsvik *et al.* 2008; Hernlund & McNamara 2015; Niu 2018; McNamara 2019). In this context, our measurements add further information on the location of such a border.

6 CONCLUSIONS

In this study, we focused on the application and expansion of a novel combined methodology, which uses reflected wave polarity and shear wave splitting, to gain information on anisotropy, mineralogy, and deformation direction in the lowermost mantle. We explore a large and complex area, located beneath the South Atlantic in proximity and within the southwestern part of the African LLSVP.

With the help of array seismology, we detected a D″ reflector over a large area beneath the South Atlantic (using PdP and SdS phases), extending the available knowledge on the geographical distribution of such a discontinuity at global level (see the reviews from Cobden *et al.* 2015; Jackson & Thomas 2021). In the regions outside the LLSVP, a D″ reflector at depth of about 2730 km causes PdP polarity variations for reflections along different directions, while the SdS reflections do not show any polarity variations. The observation of varying ScS shear wave splitting parameters suggests that azimuthal anisotropy is present in these portions of the mantle. This supports the use of the anisotropic reflections to model the polarity changes in the PdP waves. In contrast, the region inside the LLSVP, beneath the southern African border, exhibits a simple pattern of PdP reflections, a quasi-absence of reflected shear waves (only one weak SdS signal) and smaller amount of ScS splitting, suggesting a decrease in the strength of the anisotropy within the LLSVP. The reflections constrain a D″ discontinuity at a depth of about 2660 km.

These observations are modelled considering alignment of different materials expected in the D″ region, using mineral physics inputs. The diversity shown by the collected data and their geographical pattern require a regionalization in terms of mineralogy and deformation directions with two distinct domains: LPO of post-perovskite outside the LLSVP is laterally replaced by LPO of bridgmanite across the border and inside the LLSVP. The data could not locate the extension and the location of the lateral transition precisely, although with the available coverage it may occur in the vicinity of the postulated LLSVP edge, approximately beneath the mid-South Atlantic ridge. The two mineralogical and fabric domains share a common horizontal deformation direction (63° and 70° from north), pointing towards the LLSVP, but when approaching the LLSVP the deformation increases its vertical direction from 9° to 28° from the horizontal.

This work further validates the potential of the combined use of reflections and shear wave splitting to place tighter constraints on the plausible anisotropy, mineralogy and deformation scenarios in the D″ region. This approach can be improved in future work. Since finite-frequency effects and lateral heterogeneities can affect the interpretation of measured splitting parameters at long distances (e.g. Komatitsch *et al.* 2010; Borgeaud *et al.* 2016; Nowacki & Wookey 2016; Parisi *et al.* 2018; Wolf *et al.* 2022a, b), a necessary step is to perform waveform modeling of both D″ reflection and splitting, simultaneously, to further test our methodology and move towards a more precise assessment of this approach. Waveform modelling in anisotropic media with heterogeneities (e.g. Suzuki *et al.* 2021; Wolf *et al.* 2022a, b) may bring new insights into the effect of the anisotropy, also on the polarity and amplitudes of the D″ reflected waves, an approach that has not been investigated yet.

ACKNOWLEDGMENTS

We would like to thank the Editor Ian Bastow and an anonymous reviewer for their constructive comments that improved the quality of this manuscript. This project has received funding from the European Union's Horizon 2020 research and innovation program under the Marie Sklodowska-Curie Actions grant agreement No 642029–ITN CREEP and the Deutsche Forschungsgemeinschaft grant TH1530/10-2. NC and ML were funded by the US National Science Foundation via a Graduate Research Fellowship to NC (DGE-1122492) and grant EAR-1547499 to ML. Data were downloaded using ObsPy (Krischer *et al.* 2015) and were processed using freely available software such as, SAC (https://www.iris.edu/hq/), Seismic Handler (Stammler 1993), the Taup Toolkit (Crotwell *et al.* 1999) and SHEBA (https://github.com/jwookey/sheba). Vote maps were computed using the SubMachine web-based tool (Hosseini *et al.* 2018). Modelling of anisotropy was partially done using MSAT (Walker & Wookey 2012). Receiver corrections for splitting measurements were taken from the IRIS splitting database available at https://ds.iris.edu/spud/swsmeasurement. All maps were drawn using GMT (Wessel & Smith 1995).

DATA AVAILABILITY

Data were downloaded from the Data Centers at FDSN (https://www.fdsn.org/webservices/), IRIS (http://service.iris.edu) and NEIC (https://earthquake.usgs.gov/earthquakes/search/). DOI numbers are reported in the Supporting Information.

REFERENCES

Amaru, M.L., 2007. Global travel time tomography with 3-D reference models, *Geol. Ultraiect.,* **274,** 174.

Amit, H., Choblet, G., Olson, P., Monteux, J., Deschamps, F., Langlais, B. & Tobie, G., 2015. Towards more realistic core-mantle boundary heat flux patterns: a source of diversity in planetary dynamos, *Prog. Earth planet. Sci.,* **2**(26), doi:10.1186/s40645-015-0056-3.

Barruol, G. & Ben Ismail, W., 2001. Upper mantle anisotropy beneath the African IRIS and Geoscope stations, *Geophys. J. Int.,* **146**(2), 549–561.

Borgeaud, A., Konishi, K., Kawai, K. & Geller, R., 2016. Finite frequency effects on apparent S-wave splitting in the D″ layer: comparison between ray theory and full-wave synthetics, *Geophys. J. Int.,* **207**(1), 12–28.

Bullen, K.E., 1949. Compressibility-pressure hypothesis and the Earth's interior, *Geophys. J. Int.,* **5,** 335–368.

Burke, K., Steinberger, B., Torsvik, T.H. & Smethurst, M.A., 2008. Plume generation zones at the margins of large low shear velocity provinces on the core-mantle boundary, *Earth planet. Sci. Lett.,* **265,** 49–60.

Burke, K. & Torsvik, T.H., 2004. Derivation of large igneous provinces of the past 200 million years from long-term heterogeneities in the deep mantle, *Earth planet. Sci. Lett.,* **227,** 531–538.

Catalli, K., Shim, S.H. & Prakapenka, V., 2009. Thickness and Clapeyron slope of the postperovskite boundary, *Nature,* **462**(7274), 782–785.

Chandler, B.C., Chen, L.W., Li, M., Romanowicz, B. & Wenk, H.R.(2021) Seismic anisotropy, dominant slip systems and phase transitions in the lowermost mantle, *Geophys. J. Int.,* **227**(3), 1665–1681.

Chang, S.-J., Kendall, E., Davaille, A. & Ferreira, A.M.G., 2020. The evolution of mantle plumes in East Africa, *J. geophys. Res.,* **125,** doi:10.1029/2020JB019929.

Civiero, C. *et al.*, 2015. Multiple mantle upwellings in the transition zone beneath the northern East-African Rift system from relative P-wave traveltime tomography, *Geochem., Geophys., Geosyst.,* **16,** 2949–2968.

Cobden, L. & Thomas, C., 2013. The origin of D″ reflections: a systematic study of seismic array data sets, *Geophys. J. Int.,* **194**(2), 1091–1118.

Cobden, L., Thomas, C. & Trampert, J., 2015. Seismic detection of post-perovskite inside the Earth, in *The Earth's Heterogeneous Mantle: A Geophysical, Geodynamical, and Geochemical Perspective,* pp. 391–440, eds Khan, A. & Deschamps, F., Springer International Publishing.

Cottaar, S. & Romanowicz, B., 2013. Observations of changing anisotropy across the southern margin of the African LLSVP, *Geophys. J. Int.,* **195**(2), 1184–1195.

Courtillot, V., Davaille, A., Besse, J. & Stock, J., 2003. Three distinct types of hotspots in the Earth's mantle, *Earth planet. Sci. Lett.,* **205,** 295–308.

Creasy, N., Long, M.D. & Ford, H.A., 2017. Deformation in the lowermost mantle beneath Australia from observations and models of seismic anisotropy, *J. geophys. Res.,* **122**(1), 5243–5267.

Creasy, N., Pisconti, A., Long, M.D. & Thomas, C., 2021. Modeling of seismic anisotropy observations reveals plausible lowermost mantle flow directions beneath Siberia, *Geochem. Geophys. Geosyst.,* **22,** e2021GC009924, doi:10.1029/2021GC009924.

Creasy, N., Pisconti, A., Long, M.D., Thomas, C. & Wookey, J., 2019. Constraining lowermost mantle anisotropy with body waves: a synthetic modelling study, *Geophys. J. Int.,* **217,** 766–783.

Crotwell, H.P., Owens, T.J. & Ritsema, J., 1999. The TauP toolkit: flexible seismic travel-time and ray-path utilities, *Seismol. Res. Lett.,* **70**(2), 154–160.

Deschamps, F., Cobden, L. & Tackley, P.J., 2012. The primitive nature of large low shear-wave velocity provinces, *Earth planet. Sci. Lett.,* **349-350,** 198–208.

Dziewonski, A.M., Lekic, V. & Romanowicz, B.A., 2010. Mantle anchor structure: an argument for bottom up tectonics, *Earth planet. Sci. Lett.,* **299**(1), 69–79.

Ford, H.A., Long, M.D., He, X. & Lynner, C., 2015. Lowermost mantle flow at the eastern edge of the African large low shear velocity province, *Earth planet. Sci. Lett.,* **420,** 12–22.

Garnero, E.J. & McNamara, A.K., 2008. Structure and dynamics of Earth's lower mantle, *Science,* **320,** 626–628.

Garnero, E.J., McNamara, A.K. & Shim, S.-H., 2016. Continent-sized anomalous zones with low seismic velocity at the base of Earth's mantle, *Nat. Geosci.,* **9**(7), 481–489.

Garnero, E.J., Moore, M.M., Lay, T. & Fouch, M.J., 2004. Isotropy or weak vertical transverse isotropy in D″ beneath the Atlantic Ocean, *J. geophys. Res.,* **109,** doi:10.1029/2004JB003004.

Goryaeva, A.M., Carrez, P. & Cordier, P., 2015. Modeling defects and plasticity in $MgSiO_3$ post-perovskite: part 2—Screw and edge [100]dislocations, *Phys. Chem. Miner.,* **42**(10), 793–803.

Goryaeva, A.M., Carrez, P. & Cordier, P., 2016. Low viscosity and high attenuation in $MgSiO_3$ post-perovskite inferred from atomic scale calculations, *Sci. Rep.,* **6**(1), 34771.

Grand, S.P., 1994. Mantle shear structure beneath the Americas and surrounding oceans, *J. geophys. Res.,* **99,** 11 591–11 621.

Gubbins, D., Masters, G. & Nimmo, F., 2008. A thermochemical boundary layer at the base of Earth's outer core and independent estimate of core heat flux, *Geophys. J. Int.,* **174**(3), 1007–1018.

Guest, W.S., Thomson, C.J. & Spencer, C.P., 1993. Anisotropic reflection and transmission calculations with application to a crustal seismic survey from the East Greenland Shelf, *J. geophys. Res.,* **98**(B8), 14 161–14 184.

Hansen, S.E., Nyblade, A.A. & Benoit, M.H., 2012. Mantle structure beneath Africa and Arabia from adaptively parameterized P-wave tomography: implications for the origin of Cenozoic Afro-Arabian tectonism, *Earth planet. Sci. Lett.,* **319-320,** 23–34.

Hernlund, J.W. & McNamara, A.K., 2015. The core–mantle boundary region, in *Treatise on Geophysics,* 2nd edn, pp. 461–519, ed. Schubert, G., Elsevier.

Hernlund, J.W., Thomas, C. & Tackley, P.J., 2005. A doubling of the post-perovskite phase boundary and the structure of the lowermost mantle, *Nature,* **434**(7035), 882–886.

Hosseini, K., Matthews, K.J., Sigloch, K., Shephard, G.E., Domeier, M. & Tsekhmistrenko, M., 2018. SubMachine: web-Based tools for exploring seismic tomography and other models of Earth's deep interior, *Geochem. Geophys. Geosyst.,* **19,** 1464–1483.

Hutko, A.R., Lay, T., Garnero, E.J. & Ravenaugh, J., 2006. Seismic detection of folded, subducted lithosphere at the core–mantle boundary, *Nature,* **441,** 333–336.

Jackson, J.M. & Thomas, C., 2021. Seismic and mineral physics constraints on the D″ layer, in *Mantle Convection and Surface Expressions, Geophysical Monograph Series,* eds Marquardt, H., Ballmer, M., Cottaar, S. & Konter, J., John Wiley & Sons, Inc., doi:10.1002/9781119528609.ch8.

Jacobeit, E., Thomas, C. & Vernon, F., 2013. Influence of station topography and Moho depth on the mislocation vectors for the Kyrgyz Broadband Seismic Network (KNET), *Geophy. J. Int.,* **193,** 949–959.

Karato, S., 1998a. Some remarks on the origin of seismic anisotropy in the D″ layer, *Earth Planets Space,* **50,** 1019–1028.

Karato, S., 1998b. Seismic anisotropy in the deep mantle, boundary layers and the geometry of mantle convection, *Pure appl. Geophys.,* **151**(2–4), 565–587.

Karato, S. & Li, P., 1992. Diffusion creep in perovskite: implications for the rheology of the lower mantle, *Science,* **255,** 1238–1240

Karato, S., Zhang, S. & Wenk, H., 1995. Superplasticity in the Earth's lower mantle: evidence from seismic anisotropy and rock physics, *Science,* **270,** 458–461.

Karki, B.B., Wentzcovitch, R.M., de Gironcoli, S. & Baroni, S., 1999. First-principles determination of elastic anisotropy and wave velocities of MgO at lower mantle conditions, *Science,* **286**(5445), 1705–1707.

Kendall, J.M., 2000. Seismic anisotropy in the boundary layers of the mantle, in *Earth's Deep Interior: Mineral Physics and Tomography from the Atomic To The Global Scale, Geophysical Monograph Series,* vol. **117,** pp. 133–159, eds. Karato, S., Forte, A., Lieberman, R., Masters, G. & Stixrude, L., Washington, DC: American Geophysical Union.

Kendall, J.M. & Silver, P.G., 1996. Constraints from seismic anisotropy on the nature of the lowermost mantle, *Nature,* **381,** 409–412.

Kendall, J.M. & Silver, P.G., 1998. Investigating causes of D″ anisotropy, in *The core-mantle boundary region, geodynamics series, Geophysical Monograph Series,* vol. **28,** pp. 97–118, eds. Gurnis, M., Wysession, M.E., Knittle, E. & Buffett, B.A., Washington, DC: American Geophysical Union.

Kennett, B.L.N. & Engdahl, E.R., 1991. Traveltimes for global earthquake location and phase identification, *J. geophys. Int.,* **105,** 429–465.

Kito, T., Rost, S., Thomas, C. & Garnero, E.J., 2007. New insights into the *P*- and *S*-wave velocity structure of the D″ discontinuity beneath the Cocos plate, *Geophys. J. Int.,* **169**(2), 631–645.

Koelemeijer, P., 2021. Toward Consistent Seismological Models of the Core–Mantle Boundary Landscape, in *Mantle Convection and Surface Expressions,* eds. Marquardt, H., Ballmer, M., Cottaar, S. & Konter, J., doi:10.1002/9781119528609.ch9.

Komatitsch, D., Vinnik, L. & Chevrot, S., 2010. SHdiff-SVdiff splitting in an isotropic Earth, *J. geophys. Res.,* **115,** B07312, doi:10.1029/2009JB006795.

Krischer, L., Megies, T., Barsch, R., Beyreuther, M., Lecocq, T., Caudron, C. & Wassermann, J., 2015. ObsPy: a bridge for seismology into the scientific Python ecosystem, *Comput. Sci. Discov,* **8**(1), doi:10.1088/1749-4699/8/1/014003.

Lay, T., 2015. Deep Earth structure: lower mantle and D″, in *Treatise on Geophysics,* ed. Schubert, G., Elsevier.

Lay, T., Hernlund, J., Garnero, E.J. & Thorne, M.S., 2006. A post-perovskite lens and D″ heat flux beneath the central Pacific, *Science,* **314,** 1272–1276.

Li, M., 2020. The formation of hot thermal anomalies in cold subduction-influenced regions of Earth's lowermost mantle, *J. geophys. Res.,* **125,** doi:10.1029/2019JB019312.

Long, M.D. & Silver, P.G., 2009. Shear wave splitting and mantle anisotropy: measurements, interpretations, and new directions, *Surv. Geophys.,* **30**(4-5), 407–461.

Lynner, C. & Long, M.D., 2013. Sub-slab seismic anisotropy and mantle flow beneath the Caribbean and Scotia subduction zones: effects of slab morphology and kinematics, *Earth planet. Sci. Lett.,* **361,** 367–378.

Lynner, C. & Long, M.D., 2014. Lowermost mantle anisotropy and deformation along the boundary of the African LLSVP, *Geophys. Res. Lett.,* **41,** 3447–3454.

Lynner, C. & Long, M.D., 2015. Heterogeneous seismic anisotropy in the transition zone and uppermost lower mantle: evidence from South America, Izu-Bonin and Japan, *Geophys. J. Int.,* **201,** 1545–1552.

Mainprice, D., 2015. Seismic anisotropy of the deep earth from a mineral and rock physics perspective, in *Treatise on Geophysics,* ed. Schubert, G., Elsevier.

Mainprice, D., Tommasi, A., Ferre, D., Carrez, P. & Cordier, P., 2008. Predicted glide systems and crystal preferred orientations of polycrystalline silicate Mg–perovskite at high pressure: implications for the seismic anisotropy in the lower mantle, *Earth planet. Sci. Lett.,* **271**(1-4), 135–144.

Maupin, V., 1994. On the possibility of anisotropy in the D″ layer as inferred from the polarization of diffracted S waves, *Phys. Earth. planet. Inter.,* **87,** 1–32.

Maupin, V. & Park, J., 2015. Theory and observations—wave propagation in anisotropic media, in *Treatise on Geophysics,* 2nd edn, ed. Schubert, G., Elsevier.

McNamara, A.K., 2019. A review of large low shear velocity provinces and ultra low velocity zones, *Tectonophysics,* **760,** 199–220.

McNamara, A.K., van Keken, P.E. & Karato, S.I., 2002. Development of anisotropic structure in the Earth's lower mantle by solid-state convection, *Nature,* **416**(6878), 310–314.

McNamara, A.K. & Zhong, S.J., 2005. Thermochemical structures beneath Africa and the Pacific Ocean, *Nature,* **437,** 1136–1139.

Meade, C., Silver, P.G. & Kaneshima, S., 1995. Laboratory and seismological observations of lower mantle isotropy, *Geophys. Res. Lett*., **22,** 1293–1296.

Miyagi, L., Kanitpanyacharoen, W., Kaercher, P., Lee, K.K.M. & Wenk, H.R., 2010. Slip systems in MgSiO3 post-perovskite: implications for D″ anisotropy, *Science,* **329**(5999), 1639–1641.

Moulik, P. & Ekström, G., 2014. An anisotropic shear velocity model of the Earth's mantle using normal modes, body waves, surface waves and long-period waveforms, *Geophys. J. Int.,* **199**(3), 1713–1738.

Mound, J., Davies, C., Rost, S. & Aurnou, J., 2019. Regional stratification at the top of Earth's core due to core–mantle boundary heat flux variations, *Nat. Geosci.,* **12,** 575–580.

Muirhead, K.J. & Datt, R., 1976. The *N*-th root process applied to seismic array data, *Geophys. J. R. astr. Soc.,* **47,** 197–210.

Murakami, M., Hirose, K., Sata, N., Ohishi, Y. & Kawamura, K., 2004. Phase transition of MgSiO3 perovskite in the deep lower mantle, *Science,* **304**(5672), 855–858.

Ni, S. & Helmberger, D.V., 2001. Horizontal transition from fast to slow structures at the core–mantle boundary; South Atlantic, *Earth planet. Sci. Lett.,* **187** *(* 3*)*, 301–310.

Ni, S.D. & Helmberger, D.V., 2003a. Further constraints on the African superplume structure, *Phys. Earth planet. Inter.,* **140,** 243–251.

Ni, S.D. & Helmberger, D.V., 2003b. Seismological constraints on the south African superplume; could be the oldest distinct structure on Earth, *Earth planet. Sci. Lett.,* **206,** 119–131.

Niu, Y., 2018. Origin of the LLSVPs at the base of the mantle is a consequence of plate tectonics – a petrological and geochemical perspective, *Geosci. Front.,* **9,** 1265–1278.

Nowacki, A., Kendall, J.K., Wookey, J. & Pemberton, A., 2015. Mid-mantle anisotropy in subduction zones and deep water transport, *Geochem. Geophys. Geosyst.,* **16,** 764–784.

Nowacki, A., Walker, A.M., Wookey, J. & Kendall, J.M., 2013. Evaluating post-perovskite as a cause of D″ anisotropy in regions of palaeosubduction, *Geophys. J. Int.,* **192**(3), 1085–1090.

Nowacki, A. & Wookey, J., 2016. The limits of ray theory when measuring shear wave splitting in the lowermost mantle with *ScS* waves, *Geophys. J. Int.,* **207**(3), 1573–1583.

Nowacki, A., Wookey, J. & Kendall, J.M., 2010. Deformation of the lowermost mantle from seismic anisotropy, *Nature,* **467**(7319), 1091–1094.

Nowacki, A., Wookey, J. & Kendall, J.M., 2011. New advances in using seismic anisotropy, mineral physics and geodynamics to understand deformation in the lowermost mantle, *J. Geodyn.,* **52**(3-4), 205–228.

Oganov, A.R. & Ono, S., 2004. Theoretical and experimental evidence for a post-perovskite phase of MgSiO3 in Earth's D″ layer, *Nature,* **430**(6998), 445–448.

Parisi, L., Ferreira, A.M.G. & Ritsema, J., 2018. Apparent splitting of S waves propagating through an isotropic lowermost mantle, *J. geophys. Res.,* **123,** 3909–3922.

Pisconti, A., Thomas, C. & Wookey, J., 2019. Discriminating between causes of D″ anisotropy using reflections and splitting measurements for a single path, *J. geophys. Res*., **124,** 4811–4830.

Reiss, M.C., Long, M.D. & Creasy, N., 2019. Lowermost mantle anisotropy beneath Africa from differential SKSSKKS shear-wave splitting, *J. geophys. Res.,* **124,** 8540–8564.

Richards, M.A. & Engebretson, D.C., 1992. Large-scale mantle convection and the history of subduction, *Nature,* **355,** 437–440.

Ritsema, J., Deuss, A., van Heijst, H.J. & Woodhouse, J.H., 2011. S40RTS: a degree-40 shear-velocity model for the mantle from new Rayleigh wave dispersion, teleseismic traveltime and normal-mode splitting function measurements, *Geophys. J. Int.,* **184**(3), 1223–1236.

Ritsema, J., van Heijst, H. & Woodhouse, J.H., 1999. Complex shear wave velocity structure imaged beneath Africa and Iceland, *Science,* **286,** 1925–1928.

Rokosky, J.M., Lay, T. & Garnero, E.J., 2006. Small-scale lateral variations in azimuthally anisotropic D″ structure beneath the Cocos Plate, *Earth planet. Sci. Lett.,* **248**(1–2), 411–425.

Romanowicz, B. & Wenk, H.R., 2017. Anisotropy in the deep Earth, *Phys. Earth planet. Inter.,* **269,** 58–90.

Rost, S. & Revenaugh, J., 2003. Small-scale ultralow-velocity zone structure imaged by ScP, *J. geophys. Res.,* **108**.

Rost, S. & Thomas, C., 2002. Array seismology: methods and applications, *Rev. Geophys.,* **40,** 2–1-2-27.

Rost, S. & Thomas, C., 2009. Improving seismic resolution through array processing techniques, *Surv. Geophys*., **30,** 271–299.

Saki, M., Thomas, C., Merkel, S. & Wookey, J., 2018. Detecting seismic anisotropy above the 410 km discontinuity using reflection coefficients of underside reflections, *Phys. Earth planet. Inter.,* **274,** 170–183.

Savage, M.K., 1999. Seismic anisotropy and mantle deformation: what have we learned from shear wave splitting? *Rev. Geophys.,* **37,** 65–106.

Schumacher, L. & Thomas, C.(2016) Detecting lower-mantle slabs beneath Asia and the Aleutians, *Geophys. J. Int.,* **205,** (3), 1512–1524.

Schumacher, L., Thomas, C. & Abreu, R., 2018. Out-of-plane seismic reflections beneath the Pacific and their geophysical implications, *J. geophys. Res.,* **123,** 2286–2302.

Schweitzer, J., Fyen, J., Mykkeltveit, S. & Kværna, T., 2012. Seismic Arrays, in *New Manual of Seismological Observatory Practice (NMSOP-2),* ed. Bormann, P., Deutsches GeoForschungszentrum GFZ; IASPEI, doi:10.2312/GFZ.NMSOP-2⟨0:pub-id 0:pub-id-type="doi"⟩10.2312/GFZ.NMSOP-2⟨/0:pub-id⟩.

Shephard, G.E., Matthews, K.J., Hosseini, K. & Domeier, M., 2017. On the consistency of seismically imaged lower mantle slabs, *Scient. Rep.,* **7**(1), doi:10976.10.1038/s41598-017-11039-w.

Silver, P.G. & Chan, W.W., 1991. Shear-wave splitting and subcontinental mantle deformation, *J. geophys. Res.,* **96**(B10), 16429–16454.

Simmons, N.A., Forte, A.M. & Grand, S.P., 2009. Joint seismic, geodynamic and mineral physical constraints on three-dimensional mantle heterogeneity: implications for the relative importance of thermal versus compositional heterogeneity, *Geophys. J. Int.,* **177**(3), 1284–1304.

Stammler, K., 1993. Seismic handler – Programmable multichannel data handler for interactive and automatic processing of seismological analyses, *Comp. Geosci.,* **19,** 135–140.

Sun, N., Wei, W., Han, S., Song, J., Li, X., Duan, Y., Prakapenka, V.B. & Mao, Z., 2018. Phase transition and thermal equations of state of (Fe, Al)-bridgmanite and post-perovskite: implication for the chemical heterogeneity at the lowermost mantle, *Earth planet. Sci. Lett.,* **490,** 161–169.

Suzuki, Y., Kawai, K. & Geller, R.J., 2021. Imaging paleoslabs and inferring the Clapeyron slope in D″ beneath the northern Pacific based on high-resolution inversion of seismic waveforms for 3-D transversely isotropic structure, *Phys. Earth planet. Inter.,* **321,** doi:10.1016/j.pepi.2021.106751.

Tarduno, J., Watkeys, M., Huffman, T., Cottrell, R.D., Blackman, E.G., Wendt, A., Scribner, C.A. & Wagner, C.L., 2015. Antiquity of the South Atlantic Anomaly and evidence for top-down control on the geodynamo, *Nat. Commun.,* **6,** doi:10.1038/ncomms8865.

Teanby, N., Kendall, J.M. & Van der Baan, M., 2004. Automation of shear-wave splitting measurements using cluster analysis, *Bull. seism. Soc. Am.,* **94**(2), 453–463.

Thomas, C., Garnero, E.J. & Lay, T., 2004a. High-resolution imaging of lowermost mantle structure under the Cocos plate, *J. geophys. Res.,* **109**(B8), doi:10.1029/2004JB003013.

Thomas, C., Kendall, J.M. & Lowman, J., 2004b. Lower mantle seismic discontinuities and the thermal morphology of subducted slabs, *Earth planet. Sci. Lett.,* **225**(1-2), 105–113.

Thomas, C., Kendall, J.M. & Weber, M., 2002. The lowermost mantle beneath northern Asia: (1) multi-azimuth studies of heterogeneity, *Geophys. J. Int.,* **151**(1), 279–295.

Thomas, C., Wookey, J., Brodholt, J. & Fieseler, T., 2011. Anisotropy as cause for polarity reversals of D″ reflections, *Earth planet. Sci. Lett.,* **307**(3-4), 369–376.

Tommasi, A., Goryaeva, A., Carrez, P., Cordier, P. & Mainprice, D., 2018. Deformation, crystal preferred orientations, and seismic anisotropy in the Earth's D″ layer, *Earth planet. Sci. Lett.,* **492,** 35–46.

Torsvik, T.H., Smethurst, M.A., Burke, K. & Steinberger, B., 2008. Long term stability in deep mantle structure: evidence from the similar to 300 Ma Skagerrak-Centered Large Igneous Province (the SCLIP), *Earth planet. Sci. Lett.,* **267,** 444–452.

Tsuchiya, T., Tsuchiya, J., Umemoto, K. & Wentzcovitch, R.M., 2004. Phase transition in MgSiO3 perovskite in the earth's lower mantle, *Earth planet. Sci. Lett.,* **224**(3–4), 241–248.

Usui, Y., Hiramatsu, Y., Furumoto, M. & Kanao, M., 2008. Evidence of seismic anisotropy and a lower temperature condition in the D″ layer beneath Pacific Antarctic Ridge in the Antarctic Ocean, *Phys. Earth planet. Inter.,* **167**(3–4), 205–216.

van der Hilst, R.D., de Hoop, M.V., Wang, P., Shim, S.H. & Tenorio, L., 2007. Seismostratigraphy and thermal structure of Earth's core-mantle boundary region, *Science,* **315,** 1813–1817.

van der Meer, D.G., van Hinsbergen, D.J.J. & Spakman, W., 2018. Atlas of the underworld: slab remnants in the mantle, their sinking history, and a new outlook on lower mantle viscosity, *Tectonophysics,* **723,** 309–448.

Vilella, K., Bodin, T., Boukaré, Ch.-Ed., Deschamps, F., Badro, J., Ballmer, M. & Li, Y., 2021. Constraints on the composition and temperature of LLSVPs from seismic properties of lower mantle minerals, *Earth planet. Sci. Lett.,* **554,** 116685.

Walker, A.M., Dobson, D.P., Wookey, J., Nowacki, A. & Forte, A.M., 2018. The anisotropic signal of topotaxy during phase transitions in D″, *Phys. Earth planet. Inter.,* **276,** 159–171.

Walker, A.M. & Wookey, J., 2012. MSAT—a new toolkit for the analysis of elastic and seismic anisotropy, *Comput. Geosci.,* **49,** 81–90.

Walte, N.P., Heidelbach, F., Miyajima, N., Frost, D.J., Rubie, D.C. & Dobson, D.P., 2009. Transformation textures in post-perovskite: understanding mantle flow in the D″ layer of the Earth, *Geophys. Res. Lett.,* **36,** L04302, doi:10.1029/2008GL036840.

Wang, Y. & Wen, L., 2007b. Complex seismic anisotropy at the border of a very low velocity province at the base of the Earth's mantle, *J. geophys. Res.,* **112,** B09305, doi:10.1029/2006JB004719.

Wang, Y. & Wen, L.X., 2004. Mapping the geometry and geographic distribution of a very low velocity province at the base of the Earth's mantle, *J. geophys. Res.,* **109,** doi:10.1029/2003jb002674.

Wang, Y. & Wen, L.X., 2007a. Geometry and P and S velocity structure of the "African Anomaly", *J. geophys. Res.,* **112,** doi:10.1029/2006jb004483.

Weber, M., 1993. *P*- and *S*-wave reflections from anomalies in the lowermost mantle, *Geophys. J. Int.,* **115**(1), 183–210.

Weber, M. & Davis, J.P., 1990. Evidence of a laterally variable lower mantle structure from *P*- and *S*-waves, *Geophys. J. Int.,* **102**(1), 231–255.

Weber, M. & Körnig, M., 1990. Lower mantle inhomogeneities inferred from *PcP* precursors, *Geophys. Res. Lett.,* **17**(11), 1993–1996.

Weber, M. & Körnig, M., 1992. A search for anomalies in the lowermost mantle using seismic bulletins, *Phys. Earth planet. Inter.,* **73**(1-2), 1–28.

Weber, M. & Wicks, C., Jr., 1996. Reflections from a distant subduction zone, *Geophys. Res. Lett.,* **23,** 1453–1456

Wen, L., 2002. An SH hybrid method and shear velocity structures in the lowermost mantle beneath the central Pacific and South Atlantic Oceans, *J. geophys. Res.,* **107**(B3), 2055.

Wessel, P. & Smith, W.H.F., 1995. New version of the Generic Mapping Tools, *EOS, Trans. Am. Geophys. Un.,* **76**(33), 329–329.

Wolf, J., Creasy, N., Pisconti, A., Long, M.D. & Thomas, C., 2019. An investigation of seismic anisotropy in the lowermost mantle beneath Iceland, *Geophys. J. Int.,* **219,** S152–S166.

Wolf, J., Long, M.D., Leng, K. & Nissen-Meyer, T., 2022a. Sensitivity of SK(K)S and ScS phases to heterogeneous anisotropy in the lowermost mantle from global wavefield simulations, *Geophys. J. Int.,* **228**(1), 366–386.

Wolf, J., Long, M.D., Leng, K. & Nissen-Meyer, T., 2022b. Constraining deep mantle anisotropy with shear wave splitting measurements: challenges and new measurement strategies, *Geophys. J. Int.,* **230,** 507–527.

Wookey, J. & Kendall, J.M., 2007. Seismic anisotropy of post-perovskite and the lowermost mantle, in *Post-Perovskite, The Last Mantle Phase Transition, Geophysical Monograph Series,* Vol. **174,** pp. 171–189, eds Hirose, K., Brodholt, J., Lay, T. & Yuen, D., American Geophysical Union.

Wookey, J. & Kendall, J.M., 2008. Constraints on lowermost mantle mineralogy and fabric beneath Siberia from seismic anisotropy, *Earth planet. Sci. Lett.,* **275**(1-2), 32–42.

Wookey, J., Kendall, J.M. & Rümpker, G., 2005. Lowermost mantle anisotropy beneath the north Pacific from differential S-ScS splitting, *Geophys. J. Int.,* **161**(3), 829–838.

Wu, X., Lin, J.-F., Kaercher, P., Mao, Z., Liu, J., Wenk, H.-R. & Prakapenka, V.B., 2017. Seismic anisotropy of the D″ layer induced by (001) deformation of post-perovskite, *Nat. Commun.,* **8,** 14669.

Wüstefeld, A., Al-Harrasi, O., Verdon, J.P., Wookey, J. & Kendall, J.M., 2010. A strategy for automated analysis of passive Microseismic data to image seismic anisotropy and fracture characteristics, *Geophys. Prospect.,* **58**(5), 755–773.

Wysession, M.E., Lay, T., Revenaugh, J., Williams, Q., Garnero, E.J., Jeanloz, R. & Kellogg, L., 1998. The D″ discontinuity and its implications, in *The Core–Mantle Boundary Region, Geophysical Monograph Series,* Vol. **28,** pp. 273–298, eds Gurnis, M., Wysession, M.E., Knittle, E., Buffett & B.A., American Geophysical Union.

Yamazaki, D., Yoshino, T., Ohfuji, H., Ando, J.I. & Yoneda, A., 2006. Origin of seismic anisotropy in the D″ layer inferred from shear deformation experiments on postperovskite phase, *Earth planet. Sci. Lett.,* **252**(3-4), 372–378.

SUPPORTING INFORMATION

Supplementary data are available at *GJI* online.

Figure S1. Vespagram (left) and slowness-backazimuth plot (right) for the event 2015Aug26_1351 that occurred along the South Sandwich Islands subduction zone and recorded at an array (network code: YQ) in Malawi and Tanzania. The black box in the vespagram, centred around the PdP arrival, indicates the time window used to produce the slowness-backazimuth plot. The PdP wave arrives with an observed backazimuth about 3° larger (at the normalized maximum amplitude) than the theoretical backazimuth to the event (vertical dashed line). The stacked amplitude is normalized with respect to the P wave.

Figure S2. Vespagram for event 2012Jun02_0752 that occurred in South America and recorded at an array (network code: 6A) in Namibia. Shown is the variation of the PdP observed slowness (blue mark) by about 0.5 sec/deg with respect to the prediction (black mark) for the PWDK model (Weber & Davies 1990).

Figure S3. Vespagram (left) and slowness-backazimuth plot (right) for the event 2011Nov22_1848 that occurred beneath South America and recorded at an array (network code: 6A) in Namibia. The black box in the vespagram, centred around the SdS arrival, indicates the time window used to produce the slowness-backazimuth plot. The SdS phase arrives with an observed backazimuth (at the normalized maximum amplitude) corresponding to theoretical backazimuth to the event (vertical dashed line). The stacked amplitude is normalized with respect to the *S* wave.

Figure S4. Receiver and source side splitting parameters used to correct the ScS waves for upper mantle anisotropy. Receiver side fast polarizations, taken from the IRIS database (https://ds.iris.edu/spud/swsmeasurement), are indicated by the black bars centred at the seismic stations. The reference station TSUM for the splitting parameters beneath stations in Namibia (blue box) is represented in blue colour (upper right panel). Source side fast polarizations measured in this study, along the subduction zones, are indicated by the black bars which are centred at the sources and colour coded with respect to the events depth. Bar length is proportional to splitting delay time. The global map at the centre of the figure indicates the source (black stars) to receiver (black triangles) configuration and ray paths (grey lines).

Figure S5. (a) Source side shear wave splitting estimated on the direct *S* wave, while correcting for the receiver side. Top left panel shows three-component recordings. Top right panel shows uncorrected and corrected waveforms for splitting. Bottom right panel shows the error surface plot with estimated fast polarization and delay time which best linearize the elliptical particle motion shown on the bottom left. (b) D″ shear wave splitting estimated on the ScS wave, while correcting for both source and receiver. Note the elliptical particle motion of the *S* wave in (a) and the ScS wave in (b) before the analysis, and the linearized particle motion after the analysis. This event (2011Mar06_143 236) that occurred along the South Sandwich Islands subduction zone was recorded at station YNDE of the African Array (network code: AF).

Figure S6. Caption as in Fig. S5. This event (2014Feb01_03 5843) that occurred along the South Sandwich Islands subduction zone was recorded at station Z05CS of an array (network code: XK).

Figure S7. Stereonets (upper hemisphere projection) showing shear planes (great circles) and directions (black points) for *region 1-2*. Shear planes are colour coded with respect to the misfit (i.e. number of fitted observations, low misfit-high number). See also text and Fig. 7 of main manuscript.
Figure S8. Caption as in Fig. S7, but for *region 1*.
Figure S9. Pole figures of *S*-wave anisotropy and fast polarization directions (black bars) for Cases A, B and C for the relevant rotations for *region 2*. Magenta bars represent fast polarizations orientation of SK(K)S splitting from Reiss *et al.* (2019). Black bars represent fast polarizations predicted by each model. The inset in the upper left indicates pierce points of the SK(K)S phases (magenta circles) compared with the data set collected in this study for *region 2* (yellow circles) within the LLSVP.
Table S1. List of the networks used in this study.
Table S2. List of the events used in this study. Events info were taken from the National Earthquake Information Center (NEIC) catalog available at: https://earthquake.usgs.gov/earthquakes/search/.
Table S3. List of the events showing a PdP arrival. Shown are also the observed backazimuth, slowness and polarity, and the reflection point depth after back-projection (see main text, section 3.1 and Pisconti *et al.* 2019).
Table S4. List of the events showing an SdS arrival. Shown are also the backazimuth, slowness and polarity, and the reflection point depth according to the PWDK model of Weber & Davis (1990).
Table S5. Event-station information and S-ScS splitting measurements used in this study. Source corrections are estimated using the *S* waves, while receiver corrections are taken from the IRIS splitting database (IRIS DMC, 2012, Data Services Products: SWS-DBs Shear wave splitting databases, https://doi.org/10.17611/DP/SWS.1). In case of multiple available measurements for the receiver splitting, their average was used. *S* fast polarizations (ϕ'') and ScS fast polarizations (ϕ') are back-projected in the ray reference frame, at the source and D$''$, respectively, according to Nowacki *et al.* (2010).
Table S6. Elastic constants in GPa and density in kg m^{-3} used in the modelling.

Please note: Oxford University Press is not responsible for the content or functionality of any supporting materials supplied by the authors. Any queries (other than missing material) should be directed to the corresponding author for the paper.